WILEY | Hindawi

Research Article

Coordinated Control and Load Shifting-Based Demand Management of a Smart Microgrid Adopting Energy Internet

Ali M. Jasim [iD],[1] **Basil H. Jasim** [iD],[1] **Bilal Naji Alhasnawi** [iD],[2] **Aymen Flah** [iD],[3,4,5,6] **and Habib Kraiem** [iD][7]

[1]*Electrical Engineering Department, University of Basrah, Basrah 61001, Iraq*
[2]*Department of Electricity Techniques, Al-Samawah Technical Institute, Al-Furat Al-Awsat Technical University, Kufa, Iraq*
[3]*Processes, Energy, Environment and Electrical Systems (Code: LR18ES34), National Engineering School of Gabès, University of Gabès, Gabès 6072, Tunisia*
[4]*College of Engineering, University of Business and Technology (UBT), Jeddah 21448, Saudi Arabia*
[5]*MEU Research Unit, Middle East University, Amman, Jordan*
[6]*The Higher Private School of Applied Sciences and Technology of Gabès (ESSAT), University of Gabes, Gabes, Tunisia*
[7]*Department of Electrical Engineering, College of Engineering, Northern Border University, Arar, Saudi Arabia*

Correspondence should be addressed to Aymen Flah; flahaymening@yahoo.fr

High renewable energy penetration worsens systems instability. Balancing consumption energy and generation output energy reduces this instability. This paper introduces coordination control to coordinate the flow of electricity between MG buses and to stabilize the system under variable load, generation conditions. The adopted MG regulates the bidirectional DC/AC main converter using digital proportional resonant controllers in a synchronous reference frame. A maximum power point tracker-based boost DC/DC converter enables the wind turbine and solar photovoltaic to harvest maximum power. Traditional methods such as perturb and observe and incremental conductance maximum power trackers cannot solve nonlinearity and inaccurate responses. This work provides a hybrid maximum power tracker strategy to modify the responses of standard maximum power point techniques based on particle swarm optimization-trained adaptive neuro-fuzzy inference system (ANFIS-PSO) to achieve quick and maximum solar power with minimal oscillation tracking. Concerning the management system, this paper adopts a recent meta-heuristic algorithms-based DSM program to modify consumers' electricity use by shifting the load appliances to off-peak demand periods. The adopted algorithms for DSM are sparrow search algorithm (SSA), binary orientation search algorithm (BSOA), and cockroach algorithm (CA). Finally, based on energy Internet technology, ThingSpeak cloud-based MATLAB is adopted to gather and display real-time data streams and generate graphical analyses. The simulation results reveal that the recommended coordinating control produces quick grid frequency responsiveness and zero steady-state errors. The optimal demand management program minimizes peak energy consumption from 5.2 kWh to 4.6 kWh. All DSM methods cost 439.1 $ per month, compared to 484.4 $ for the nonscheduling load profile.

1. Introduction

1.1. Background, Challenges, and Motivation. The operation of microgrids (MGs) requires the balancing of consumption and production powers. The continuously increasing and changing load demand affects overall system stability. Thus, the demand-generation imbalance causes system voltage and frequency to deviate from their nominal points. Next, system stability must be continuously tracked by the control structure to get rid of these dilemmas. So, there should be a match between energy usage and its supply to benefit from its advantages. Due to the problems of increasing reliance on energy, the duties of energy managers are now more difficult than they were before. Consequently, MGs are installed to

maximize the benefits from the generation side and minimize peak demand hour usage by managing the demand side [1, 2].

Energy use has led to the depletion of fossil fuels, including petroleum, natural gas, and coal. Additional greenhouse gases will be released as a result. Renewable energy resources (RERs) such as solar photovoltaic (PV), biomass, tidal, and wind energy are being integrated into energy systems all over the world to solve the above problems. MGs may reduce pollution and provide uninterrupted power to the community. MGs switch between isolated and grid-connected modes [1, 2]. Standalone, isolated, or autonomous MGs are considered self-sustaining [3]. MG generates power in isolated mode, and energy storage systems (ESSs) may stabilize energy demand. MG and the utility may share the auxilary services [4]. Figure 1 depicts MG's central controller managing loads and producing units. Figure 1 shows many resources connected to the electrical main grid. The power conversion interface transfers power from the MG switching regulator to the required voltage and frequency. The central control unit controls these electronic connections locally. The energy Internet (EI), inspired by information and communications network technologies, aims to achieve RER-based electrification goals. EI includes advanced power and electronics, information, intelligent management, new power networks, and Internet of Things (IoT). Energy flows in both directions via the energy nodes' dynamic links. Due to advances in technology, hybrid renewable energy systems are becoming more and more popular for power generation. These systems are interesting because many sources may work together to supply more reliable energy to end-users than a unified power system. To increase the reliability of the power supply, wind turbines (WT) and solar PV systems must be compatible with more ESSs. The MG may be studied using residential building resources including conventional energy sources, ESSs, RERs, regulating techniques, and demand-side management (DSM) [3, 4].

Integration of power systems with inverter-based distribution generators may be accomplished by a variety of control approaches, including proportional-integral (PI) controllers, deadbeat controllers, hysteresis, and proportional resonant (PR) controllers. Despite the ease of use and responsiveness of hysteresis control, the output response has huge ripples, which leads to subpar stream quality and causes challenges when designing the output filter [5]. Since deadbeat predictive control is compatible with currently controlled distribution generators, its application has become widespread. It is complex and system dependent [6]. Since current-controlled generators are suitable with deadbeat predictive control, it has become widespread in applications. It is complex and system-dependent [6]. Unlike PI controllers, digital PR control reduces steady-state error, rectifies numerous harmonics underlying sinusoidal signals, and regulates them. However, the PI controller is very complex and depends on system parameters [6]. For optimal parameter selection in PI controllers, optimization algorithms and artificial intelligence are required to be used, but doing so will make the control mechanism complex. This confirms the need to calculate control parameters for a simple system [7].

Due to the rapid depletion of traditional resources, the need for RER is developed exponentially. Compared to other RERs, the PV system has made exceptional progress over the past decade [8]. Due to the nonlinear voltage and current characteristics of solar PVs, they have a limited ability to customize. The maximum power point trackers (MPPTs) are essential for maximizing solar PV energy production under global MPPT circumstances. Numerous MPPT control approaches are investigated in [9–11]. In [12–14], traditional MPPT techniques (perturb and observe (PO) and incremental conductance (INC)) are described. The PO and INC approaches are simpler to apply, but they include considerable oscillations at the maximum power point (MPP), resulting in power losses. The INC algorithm is precise and reactive under changing atmospheric circumstances. Yet, modeling and execution are difficult. However, the previous methods are inefficient when exposed to variable solar irradiance and when calculating perturbation magnitude. Thus, MPPT trackers based on fuzzy logic control (FLC) and neural networks (NNs) have been used to solve the shortcomings of classic MPPT algorithms [15]. Since it solves uncertainty and non-linearity difficulties, fuzzy logic-based MPPT is crucial. Expertise and rule base systems hamper FLC design. The ANN technique, which uses multilayered neurons instead of standard algorithms, is utilized for fast PV power tracking under variable conditions. After merging ANN and FLC, a hybrid algorithm with appealing learning abilities may be employed to teach MPPT members. Designers struggle to teach and update ANFIS standards on time. Recent artificial intelligence algorithms such as PSO, the ant colony optimization (ACO), artificial bee colony (ABC), and genetic algorithm (GA) tackle optimization problems [16–19]. As the solar radiation level fluctuates, the NN and FLC can monitor PV better than only the FLC. PSO is a great option for fluctuating weather and several peaks that make it hard to access the MPP region. PSO is simpler to implement than the other optimization techniques. Compared to optimization techniques, it tracks PV power quickly and accurately under various operating situations. PSO update is simpler and faster than gradient techniques [20]. References [21, 22] related to MPPT only, and their authors proposed a hybrid MPPT method that combines classical PO technology with modified invasive weed optimization (MIWO) under partial shade scenarios and rapidly changing weather to achieve efficient extraction of the maximum power from the PV-based hybrid system. This ensures both faster convergence and a better search for global maxima of power under the mentioned conditions. Compared to some existing techniques, the results of these studies clearly show the superior performance of the introduced methodology.

MG may reconstruct infrastructure, regulate dispersed energy resources, and supervise the power market. Network's conversion to MG empowered a recent DSM era. DSM can improve network efficiency, reduce energy harvesting costs, reduce load pressure, improve the reliability, and improve capacity without manipulating the physical
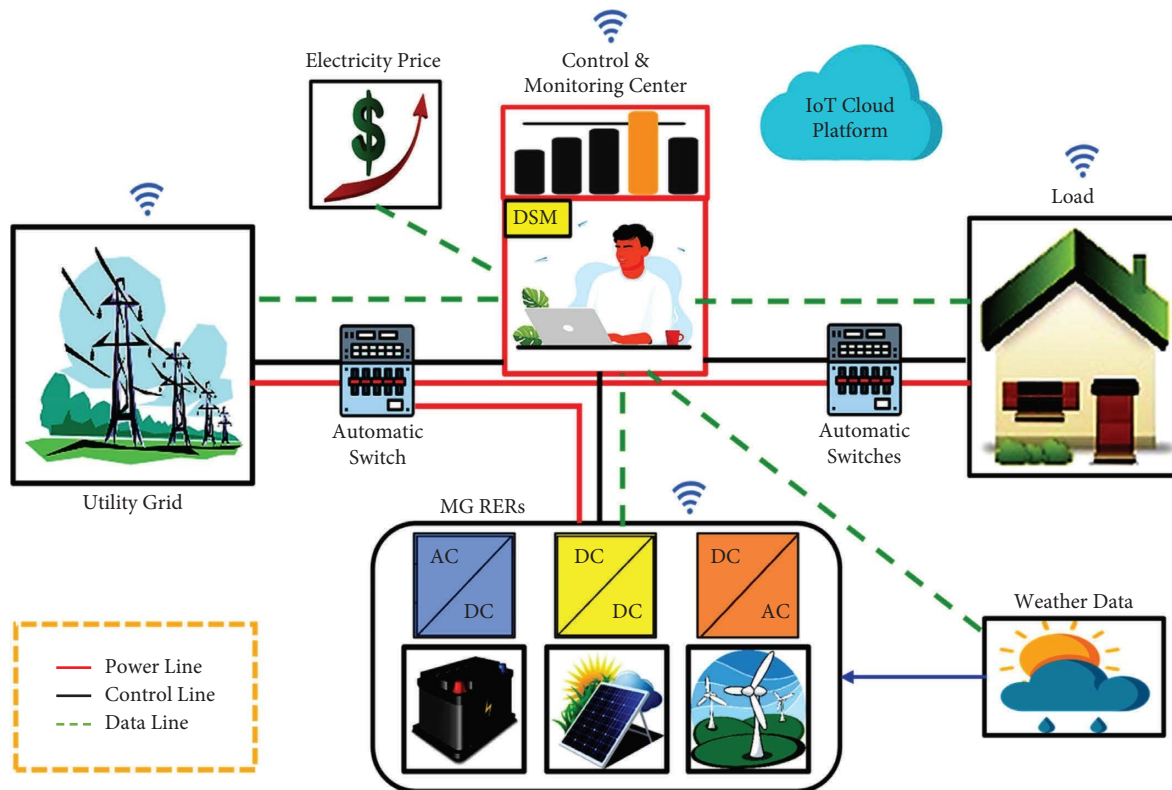
FIGURE 1: MG and power control management integration.

design of the power system. Moreover, MG and DSM reduce carbon emissions to fight global warming. By lowering carbon emissions and consumption costs, MG and DSM can help residents build smart, sustainable, and economically viable communities. Smart MGs are the building blocks of an EI since they may be islanded or grid-connected and the IoT connects things across any power infrastructure. Smart meters let EI monitor household energy use in real time. Electric loads, RERs, and storage systems connected to power suppliers and consumers form the EI concept. Real-time power and data transfers make the EI innovative. Smart MGs, storage, vehicle-to-grid, and other green technology may cause this shift [1].

The purpose of this study is to investigate and analyze the integration of AC/DC MG hybrid control, optimized DSM, and EI-based monitoring into a comprehensive MG-based system. This system is discretely controlled to operate in both grid-isolated and grid-tied modes, achieving maximum PV power using novel MPPT technique, and optimally managing the load demand using optimal time-shifting-based load appliances. It can be remotely monitored through EI technology by using a secure IoT-based platform. Table 1 contains this study's nomenclatures and abbreviations.

1.2. Literature Review. Several earlier studies in the literature have proposed MG coordination control strategies. Reference [23] suggested and explored a PV power coordination control strategy for MG. It investigated how PV cells work and how the MPPT and restricted power mode switch work.

AC bus wire, DC bus voltage, and frequency stability approaches are investigated. A coordination control approach for supply-side distributed generators (DGs) and demand-side load resources was presented in [24]. First, by pooling together adaptable loads, an MG model is created with high penetration DGs, taking into account virtual power plants (VPPs). Next, DGs and VPPs in steady operation, unexpected load disturbances, and inadvertent DG failures are coordinated using a control framework. For the coordinated design of power system stabilizers and the controllers, the publication [25] provided an efficient hybrid optimization approach based on pattern search and a chaotic sine cosine algorithm. The controller parameters are used as choice variables in an optimization model of the design issue. In the work [26], a control system that enables the DC link of a smart transformer (ST) to be coupled with distributed generating sources and storage systems is used. This feature allows the ST to continue supplying power to connected applications in emergency situations, such as power outages. The control technology used can both mitigate the power grid's harmful harmonics and correct the imbalance.

A control strategy for a RERs-based MG that can run in both off-grid and grid-connected modes was proposed in reference [27]. The RER controllers detect islanding, at which point the MG enters voltage control mode (VCM). In on-grid mode, the interface control supplies active and reactive power to the grid. An islanding detection technique will convert the inverter to VCM after proper resynchronization without harming critical loads. In [28], the authors implemented a management system that switches between

TABLE 1: Study's nomenclatures and abbreviations.

Abbreviations	
ANFIS-PSO	Particle swarm optimization-trained adaptive neuro-fuzzy inference system
SSA	Sparrow search algorithm
BSOA	Binary orientation search algorithm
CA	Cockroach algorithm
MG	Microgrid
RERs	Renewable energy resources
PV	Photovoltaic
ESSs	Energy storage systems
EI	Energy internet
WT	Wind turbine
DSM	Demand-side management
PR	Proportional resonant
PI	Proportional integral
MPPTs	Maximum power point trackers
PO	Perturb and observe
PWM	Pulse width modulation
CSO	Cockroach swarm optimization
INC	Incremental conductance
MPP	Maximum power point
FLC	Fuzzy logic control
NNs	Neural networks
ACO	Ant colony optimization
ABC	Artificial bee colony
GA	Genetic algorithm
IoT	Internet of thing
VPPs	Virtual power plants
ST	Smart transformer
VCM	Voltage control mode
POSLLC	Positive output super lift Luo converter
PAR	Peak-to-average ratio
RTP	Real-time price
API	Application program interface
SOC	State of charge
CCM	Boost continuous conduction mode
Nomenclatures	
k_P	The proportional gain
k_R	The resonant parameter gain
ω_o	The controller's resonance frequency
$G_{PR}(s)$	Unideal PR controller transfer function
ω_c	The resonant bandwidth orbits AC frequency
f_{bw}	The resonance frequency bandwidth
f_g and f_r	The grid and resonant frequency
T	The sampling time
$G_R(z)$	The transfer function of discrete resonant IIR filter
a_0, a_1, a_2	The parameters of the feedforward path of the filter
b_0, b_1, b_2	The parameters of the feedback path
$u(n)$ and $y(n)$	The resonance filter's input and output
H_i	The gauged current gain
R_0 and L_o	The inverter's line resistance and inductor
ζ	The damping factor
B_r	The resonance bandwidth
ω_r	The resonance frequency
T_a	Sampling interval
k_r	The resonance control parameter
V_{dc}	The inverter's DC input voltage
V_I and I_I	The voltage and current of the inverter
$I_d, I_q, I_{dref},$ and I_{qref}	The measured and reference inverter output current in dq-frame
k_{Pc} and k_{Rc}	The proportional and resonant gains of the PR current controller
V_d and V_q	The measured inverter output voltage in dq-frame
V_{dref} and V_{qref}	The reference inverter output voltages in dq-frame

TABLE 1: Continued.

k_{Pv} and k_{Rv}	Proportional and resonant gains of PR voltage controllers
x and y	The variables of ANFIS input
A_i and B_i	The variables of fuzzy system
f_i	The fuzzy sets' outputs
r_i, k_i, p_i	The ANFIS system's design parameters
$\mu_{Ai}(x)$ and $\mu_{(Bi\text{-}2)}(y)$	Fuzzy membership functions
cn_i, d_i and g_i	The center, the breadth, and the fuzzy factor of membership function
$\overline{W}_i$	The layer 3 output
X^k	Swarm location vector of PSO
V^k	Swarm velocity vector of PSO
D	Dimensional space
P^z	The optimal location reached by the swarm's particles
c_1 and c_2	Positive constant (individual and global) learning rates
r_1 and r_2	Random values between 0 and 1
χ	The constriction factor
$\text{Out}_{\text{PO,MPPT}}$ and $\text{Out}_{\text{INC,MPPT}}$	The output signals of hybrid PSO-based ANFIS and PO and INC techniques
Out_{PO} and Out_{INC}	The output signals of PO and INC techniques
$\text{Out}_{\text{ANFIS}}$	The output signals of PSO-based ANFIS MPPT
V_1 and V_2	The DC/DC converter's output and input voltages
η	The converter efficiency
ΔI	Estimating inductor ripple current
$I_{2,\max}$	The maximum output current
L	The inductor value
f_s	The switching frequency
C_{out}	The minimal output capacitance
ΔV_2	Output voltage fluctuation
C_{in}	Minimum input capacitance
ΔV_1	Change in the input voltage
t	Time slots
N_{SL}	The total number of shiftable appliances
$A_{\text{SL}}(r,t)$	The power used by a shiftable appliance r during t-time
T_1 and T_2	The shift's beginning and finishing times
Z_{SL}	The ON/OFF status of a shiftable appliance
$E_{\text{SL}}(t)$	Overall energy usage of shiftable loads
$C_{\text{SL}}(t)$	The daily cost of consumption for shiftable appliances
$\text{Pr}(t)$	The electrical tariff price
$E_{\text{NSL}}(t)$	Overall energy usage of nonshiftable loads
$Z_{\text{NSL}}(u,t)$	The ON/OFF status of a nonshiftable appliance
N_{NSL}	The total number of nonshiftable appliances
$A_{\text{NSL}}(u,t)$	The power used by a nonshiftable appliance r during t-time
$C_{\text{NSL}}(t)$	The daily nonshiftable appliance operating expenditures
$E_T(t)$	The total energy consumption
$A(m,t)$	The daily load demand usage after scheduling has occurred
$B(m,t)$	The daily load use before scheduling has occurred
$S(t)$ and $H(t)$	The shifted and shiftable appliances' powers
Z	Sparrow positions matrix
n	The sparrow count
d	The variable's dimension
$F(Z)$	The fitness vector for all sparrows
$Z_{i,j}^{k+1}$	Each iteration's sparrow finder location
$Z_{i,j}^k$	The current position of the sparrow finder
k	The recent iteration
$\text{iter}_{\max}$	The highest number of iterations allowed
α and Q	Random and normal-distributed random integers
ST and R	The alarm and safety limits
Z_{worst}^k	The current search space's worst position
Z_p^k	The occupied optimal position
A^+	A random factor of size d with entries randomly distributed between [1, 1]
Z_{best}^k	The current best global position
β	The step size control parameter
K	A random sparrow movement between -1 and 1

f_i, f_g, and f_w	The world's current, optimum, and worst levels for sparrow fitness
ε	The lowest constant needed to avoid a zero-division mistake
Z_i	The players' starting positions of BSOA or the cockroach position
z_h^d and z_l^d	The maximum and minimum limits
$dZ^{j,d}$	BSOA probability function
q_i	Referee's hand direction
P_i	The optimal local solutions for the strongest cockroaches
P_g	The global optimum position in CSO
p_i	The individual's perfect position in CSO

distributed energy and generation resources. This system includes MPPT controllers, battery charge/discharge controllers, and an DC/AC converter to balance load needs and supply availability. The MPPT method is applied to the solar PV in order to gather a maximum amount of power when the climate changes. The authors of [29] suggested a co-ordination control of hybrid AC/DC MG with MPPT-based boost converter using the PO method and fuzzy-based MPPT. The DC/DC and DC/AC power converters were managed by PI controllers. This reference demonstrates the significant drawbacks of the PO technique, which causes the output power to oscillate around the MPP stable operation, resulting in rippling converter output results, and tracks in the reverse direction, far from the MPP, when solar radiation levels are rapidly increasing or decreasing. In [30], PO and INC were compared, and it was decided that both are superior for determining the maximum power to be forwarded to the user. It was observed that the method of INC provided smoother outputs for changes, unlike the PO method, which was not able to follow faster changes such as irradiation and temperature change. The authors of [31] proposed co-ordinated control for MG in grid-tied and off-grid modes using hybrid power generation and variable loads. The proposed MG allows for the consistent operation of dispersed energy resources to provide active power and auxiliary service as required. Inevitably, energy injection or reduction is needed to maintain grid power balance because the power produced by wind and solar renewables is intermittently greater or less than demand [32].

Numerous coordination control techniques based on PI, hysteresis, PR controllers, and deadbeat controllers can be adopted to interface power inverters with the power system [5–7, 33–35]. While the PR control method is often employed to rectify the sine signals harmonics and minimize steady-state error, PI regulators provide greater error and are consistent with the parameter-adjusting issue [33]. A single-phase inverter prototype and a DC-DC positive output super lift Luo converter (POSLLC) are proposed in the topology of reference [36] for transmitting electricity from a solar module to the main grid. Maximum output power and efficiency are achieved by fine-tuning the voltage from the PV panels, the current flowing via a DC-DC converter's inductor, and the current injected into the grid. Reference [37] introduces a hybrid DC MG with an improved power management control strategy. Depending on the voltage, electrolyser, and fuel cell, the introduced control scheme is able to improve the DC-link voltage dynamics and enhance

power management between every source, generation, and load. This study adopts the PO technique for MPPT. To improve the voltage's transient response, the battery PI-controller gains are dynamically set using the Takagi–Sugeno fuzzy control according to the voltage deviation and its derivative. In this regard, the authors of [38] studied the stability of control exchanges in a parallel system with two inverters adopting high-voltage DC connections. Li et al. presented a technique for controlling a multi-infeed inverter connected to an AC grid in [39]. This system can keep the balance of active power between the load and supply. The authors of [40] proposed a control method for parallel inverters based on dq-axes currents control. This control scheme is based on PI-based multivariate decentralized controllers, which ensure step-tracking reference signals and stability with no steady-state errors. The authors of [41] adopted PR controllers only for on-grid applications to accurately coordinate the power flow between the utility and DGs. The control strategy adopts a systematic method to select the parameters of the controllers.

It essentially entails managing or modifying the load demand to enhance the load factor when designing the MG. All of the MGs described above were proposed without implementing the DSM program, which would have helped reduce energy consumption, lower electricity costs, and achieve load/demand balance. A multiobjective optimization issue may incorporate binary contributing elements with load connection/disconnection to reduce operational expenses and load shifting/curtailing annoyance. A DSM approach based on peak clipping and load shifting was presented in [42]. The suggested method was simulated in MATLAB/Simulink R2021a and then optimized using the artificial NNs. An MPC-based DSM is proposed in [43] with peak shift restrictions, and a mechanism based on aggregates and load curtailment is presented in [44] to encourage the short-term lowering of electricity demand during predetermined hours. Using meta-heuristic optimization algorithms for DSM, the authors of [45, 46] consider a dispatch algorithm to strike a balance between demand and load. In [47], the crow search and gray wolf optimization algorithms were utilized to construct a framework for residential appliance scheduling. The suggested technique evaluates the price of power savings, comfort for users, and peak-to-average Ratio (PAR) reduction for household appliances given the availability of real-time pricing information. Other optimization algorithms can be used to execute an optimal DSM program, including an efficient

population-based optimization algorithm such as the golden search optimization, gravitational search algorithm, gray wolf optimization, sine-cosine algorithm, and tunicate swarm algorithm, which are mentioned in the study [48]. The relevant prior studies are summarized in Table 2. The literature presented in this section and briefly compared in Table 2 has yielded relatively good research results, but the literature has not studied comprehensive systems that include control, management, and cyber layers. Especially, the previous literature described control or management, so this study includes coordinating control as well as optimal demand management, which are not presented in the literature in the comprehensive system according to the authors' knowledge.

1.3. Paper Contributions. As far as the authors are aware, no previous study has addressed the integration of hybrid AC/DC MG control, optimum DSM, and EI-based monitoring into a comprehensive MG-based system. This work offers a discrete control approach for inverters based on PR regulators for islanded and grid-connected MG in order to enhance transient power flow, remove steady-state errors, and provide a rapid transient response. To our knowledge, this is the first study to propose adapting PO and INC MPPTs-based response by employing ANFIS trained by the PSO algorithm in order to extract MPP. Moreover, this paper considers residential energy consumption management based on an optimal DSM controller using a load appliances-shifting technique. Our model utilizes SSA, BOSA, and CSO optimization algorithms. The selected algorithms are appraised based on their simplicity of application and recentness (BSOA [49]), and substantial benefits, such as low parameter count, quickly converge, and resistance to being "stuck" in a local optimal solution (SSA [50]). CSO is simple and efficient, solving global optimization issues [51]. The energy Internet uses ThingSpeak to track significant discoveries. The study's main contributions are as follows:

(1) This study presents a combination of AC/DC islanded and grid-tied MG powered by renewable and stored energies to minimize DC/AC/DC power electronic conversions. The proposed system handles the coordination of power flow across buses to sustain a demand-supply balance and to ensure the stability of the system under a diversity of generation and load conditions. The approved MG is applied to the planned control, management, and monitoring subsystems as a whole.

(2) In this study, an inverter controlled by a discrete PR controller is designed. The resonance path coefficients, resonant, and proportional gains are all determined methodically. It helps researchers develop digitally controlled inverters. A frequency-domain study of the PR controller has been included. Unlike the classical PI controller, the adopted PR controller pursues the reference signal rapidly, adapts to varying grid frequencies, is easy to setup, and has no steady-state error.

(3) The MPPT is integrated into the boost converter used for solar PV and wind energy systems. Novel MPPT techniques are proposed to modify the outputs of PO and INC algorithms using hybrid PSO and ANFIS for rapid PV power tracking with minimum oscillations.

(4) Based on effective optimization algorithms (CSO, BOSA, and SSA), an optimal MG load-shifting DSM strategy has been presented. Real-time price (RTP) is used to offer dynamic pricing and an interactive market for managing load, which helps consumers save energy costs.

(5) By combining embedded systems and IoT applications, the in-built demand for consumption can be controlled. This study proposes continuous load monitoring and scheduling. EI and the ThingSpeak platform provide real-time tracking of energy expenditures.

1.4. Paper Organization. The paper continues as follows: a proposed MG structure is presented in Section 2. In Section 3, the proposed optimal DSM approach is described. The system's performance results are illustrated in Section 4. The last Section of the study discussed the conclusion.

2. Proposed MG System

Three layers make up the proposed MG system. Figure 2 represents the system's layers. The first is the physical layer, which is comprised of power electronics converter-based RERs such as WT, solar PV, and storage batteries. The control layer comprises the control technique related to every power converter. WT and solar PV use the MPPT technique to maximize their power production. An ANFIS-based PSO MPPT technique is used to adapt the outputs of INC and PO techniques to get maximum solar PV power without oscillation under changes in load or solar radiation. The main bidirectional DC/AC inverter is controlled by a PR controller-based discrete control. This controls the MG in both of its operating modes (grid-connected and islanded modes). Battery charging and discharge are controlled using a PI controller-based buck-boost converter. The DC bus voltage must maintain stable at 400 V. Adopted load is supported by an optimum DSM based on modern SSA, BSOA, and CSA algorithms to shift shiftable load from peak hours to nonpeak hours to minimize peak consumption and energy costs and improve load factor. The last layer is the monitoring layer, which is helpful for monitoring the functioning of the system via the use of energy Internet technology and ThinkSpeak platform.

The open-source IoT framework ThingSpeak platform and MATLAB-processing program exchange data to simulate proposed communication architectures. The ThingSpeak was chosen to simulate real-time cloud communication because of the following advantages [52]:

(1) Aggregation on the ThingSpeak IoT platform, monitoring, and analysis of data. In the smart MG

TABLE 2: A brief summary of the relevant literature.

Reference no	Year	Coordination control	MPPT	ON/OFF-grid MG	Using DSM	Optimization algorithms-based DSM	Access to Internet
[21]	2020	NO	YES	OFF-grid	NO	NO	NO
[22]	2021	NO	YES	OFF-grid	NO	NO	NO
[23]	2022	YES	YES	ON-grid	NO	NO	NO
[24]	2022	YES	NO	OFF-grid	NO	NO	YES
[25]	2022	YES	NO	NO	NO	NO	NO
[26]	2021	YES	YES	ON-grid	NO	NO	NO
[27]	2020	YES	NO	ON/OFF-grid	NO	NO	NO
[28]	2020	YES	YES	ON-grid	NO	NO	NO
[29]	2022	YES	YES	ON/OFF-grid	NO	NO	NO
[30]	2013	NO	YES	OFF-grid	NO	NO	NO
[31]	2020	YES	YES	ON/OFF-grid	NO	NO	NO
[32]	2017	YES	NO	OFF-grid	NO	NO	NO
[33]	2018	YES	NO	ON-grid	NO	NO	NO
[34]	2023	YES	YES	ON-grid	YES	NO	NO
[35]	2014	YES	NO	ON-grid	NO	NO	NO
[36]	2021	YES	YES	ON-grid	NO	NO	NO
[37]	2017	NO	NO	OFF-grid	NO	NO	NO
[38]	2016	YES	NO	ON-grid	NO	NO	NO
[39]	2010	NO	NO	OFF-grid	NO	NO	NO
[40]	2020	YES	NO	ON-grid	NO	NO	NO
[41]	2022	YES	NO	ON-grid	NO	NO	NO
[42]	2022	NO	NO	ON-grid	YES	YES	NO
[43]	2019	NO	NO	ON-grid	YES	NO	NO
[44]	2020	NO	NO	ON-grid	YES	NO	NO
[45]	2022	YES	NO	ON-grid	YES	YES	NO
[46]	2022	NO	NO	ON-grid	YES	NO	YES
[47]	2020	NO	NO	ON-grid	YES	YES	NO
[48]	2022	NO	NO	NO	NO	NO	NO
Current work	2023	YES	YES	YES	YES	YES	YES

paradigm, many ThingSpeak channels monitor the power profile in real time and display it visually.

(2) Security: there is a unique identifier for every channel and may be accessed with a username and password. Each application programming interaction channel has two keys. Application program interface (API) write and read keys are randomly generated. These keys store and retrieve channel data through the Internet.

(3) It provides real-time data and remote control interchange between the virtual device and the user.

(4) Internet-based data exchange between MATLAB and ThingSpeak.

(5) Allow simultaneous data input, export, analysis, and visualization across platforms and fields.

The details of the proposed components-based MG are illustrated in Figure 3. In the MG system, there are three adopted DC-DC converters, one for every generation unit. The DC-DC boost converters are used for the WT and solar PV, and the buck boost converter is used for the ESS. MPPT algorithms control the boost converters. The battery bidirectional converter is controlled to maintain a stable DC bus during charging and discharging. The main bidirectional converter is a DC/AC inverter. This inverter is controlled to manage power flow, stabilize the AC bus, and enable the MG to operate in either islanded or grid-connected mode. Also, this study investigates the load-shifting-based DSM to manage the load, reduce peak consumption, reduce costs, and improve the load factor.

2.1. The Control Methods

2.1.1. DC/AC Inverter Control Method.
The main inverter is controlled by discrete PR controllers, as illustrated in Figure 4, for both the selected control techniques in grid-connected or island mode of operation. The authors of [34, 41] presented the modeling of the PR controller, which is introduced as follows.

The transfer function of the idealized PR controller is provided by the following equation:

$$G_C(s) = k_P + \frac{k_R s}{s^2 + \omega_o^2}, \tag{1}$$

where k_P represents the proportional gain of the controller, k_R represents the resonant parameter gain, and ω_o acts the controller's resonance frequency, which is the frequency of the main grid $(2\pi \times 50)$.

Realizing the perfect PR controller is challenging because it behaves like a system with an unlimited quality factor. Consequently, the following is an unideal PR controller transfer function:
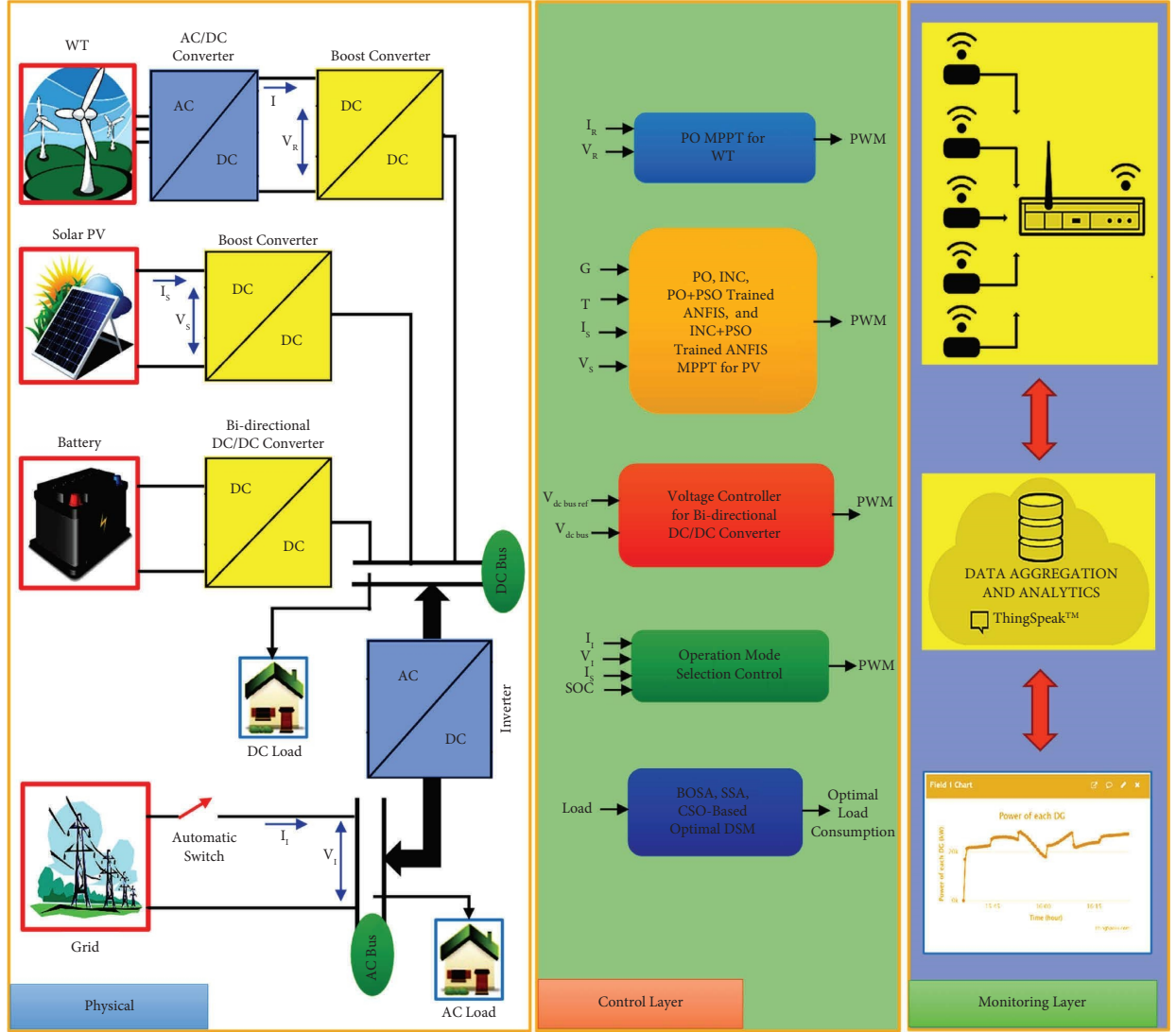
FIGURE 2: The proposed layers-based MG.

$$G_{PR}(s) = k_P + \frac{2\omega_c k_R s}{s^2 + 2\zeta\omega_c s + \omega_o^2}, \tag{2}$$

where $\omega_c = 2\pi f_{bw}$ denotes the resonant bandwidth orbits AC frequency $\omega_o = 2\pi f_r$ or $\omega_o = 2\pi f_g$, f_{bw} represents the resonance frequency bandwidth, and f_g and f_r are the grid and resonant frequency.

Tustin frequency prewrapping is used in the inverter's control approach of a MG equipped with a discretized PR controller. Analog control discretization can be investigated by adopting Tustin's technique [53]. This relation substitutes the analog controller S-domain with Z-domain.

$$s = \frac{2(z-1)}{T(z+1)}, \tag{3}$$

where T represents the sampling time.

$$G_{PR}\left(\frac{2(z-1)}{T(z+1)}\right) = k_P + \frac{2\omega_c k_R(2(z-1)/T(z+1))}{(2(z-1)/T(z+1))^2 + 2\zeta\omega_c(2(z-1)/T(z+1)) + \omega_o^2} = k_P + k_R \times G_R(z). \tag{4}$$

The resonant pathway is characterized by the transfer function in z-domain ($G_R(z)$), which is identical to the resonant gain and discrete resonant IIR filter.

$$G_R(z) = \frac{b_2 z^{-2} + b_1 z^{-1} + b_0}{a_2 z^{-2} + a_1 z^{-1} + a_0}, \tag{5}$$
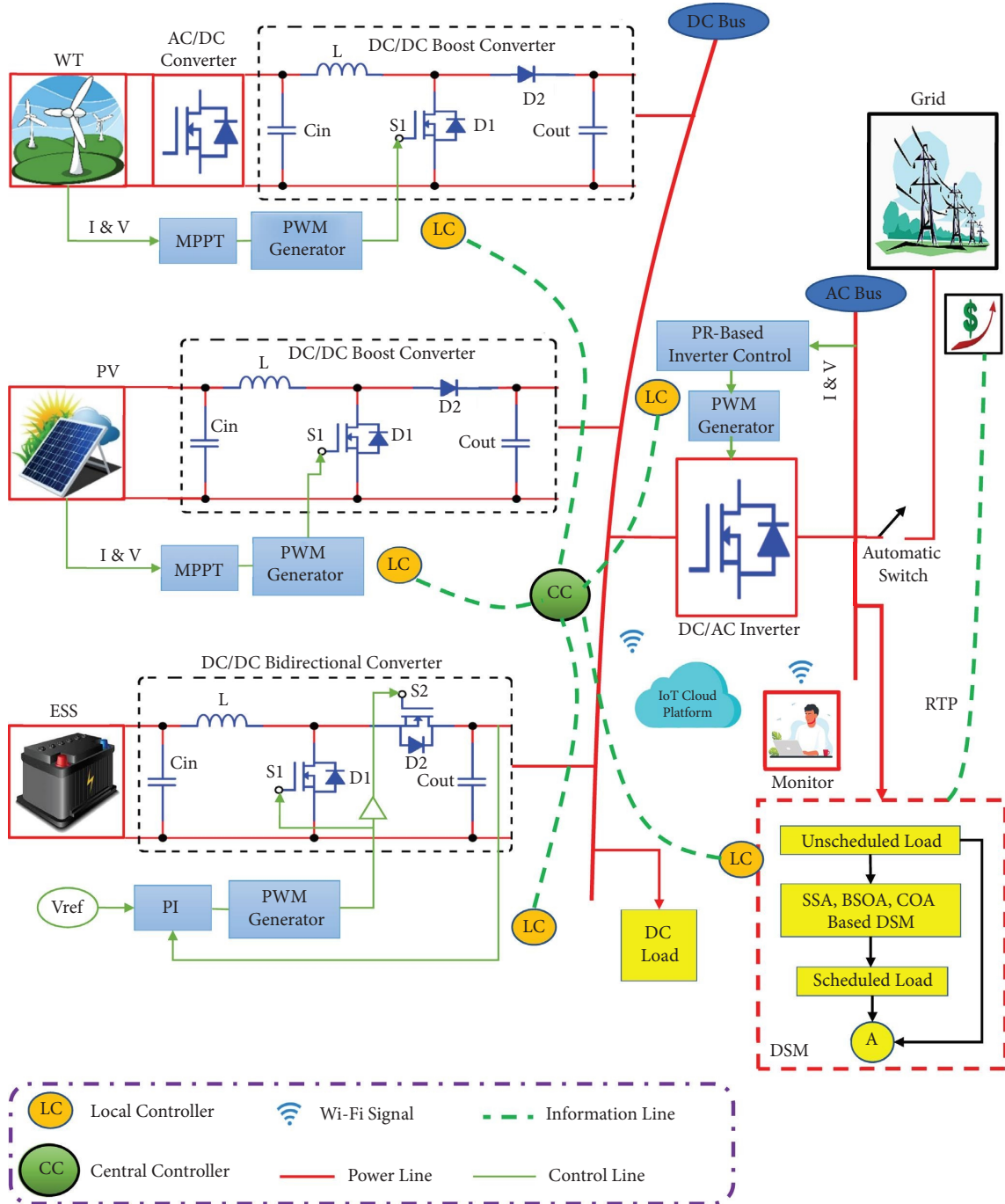
FIGURE 3: The details of proposed components-based MG.

where b_0, b_1, b_2 denote the parameters of the feedback path and a_0, a_1, a_2 denote the parameters of the feedforward path of the filter. It should be noticed that a_0 is set to "1" on

purpose so that the resonant filter transfer function in equation (5) may be recast as a difference formula by [54]:

$$y(n) = b_0 \times u(n) + b_1 \times u(n-1) + b_2 \times u(n-2) - a_1 \times y(n-1) - a_2 \times y(n-2), \qquad (6)$$
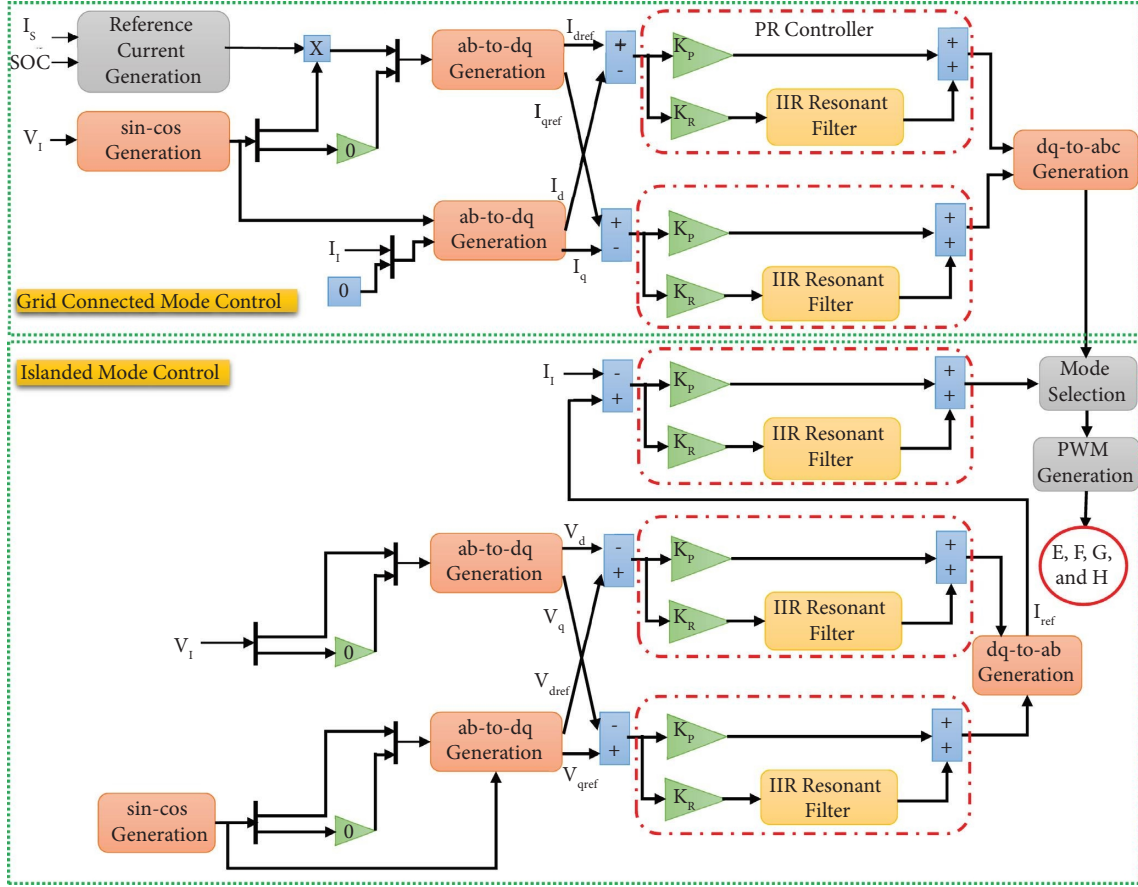
FIGURE 4: The proposed PR controller-based discrete control of the MG inverter.

where the resonance filter's output is denoted by $y(n)$, while its input is denoted by $u(n)$. This step can be viewed as a significant contribution to the overall significance of this effort. The most crucial factor to consider is selecting the resonant frequency since it determines the controller's frequency to reach steady-state zero error. The designer may derive filter coefficients from the required filter frequency response in the s-domain. Equations (7)–(15) then yield the resonant and proportional gains and digital implementation coefficients [55].

$$k_P = \frac{\omega_r \times L_o \times (2\zeta + 1) \times (\sqrt{2\zeta + 1}) - R_0}{H_i \times V_{\mathrm{dc}}},\tag{7}$$

$$k_R = \frac{\omega_r^2 \times L_o \left[(2\zeta + 1)^2 - 1\right]}{2 \times H_i \times V_{\mathrm{dc}}},\tag{8}$$

$$b_0 = T_a \times k_r \times B_r,\tag{9}$$

$$b_1 = T_a\left[-C - B_r \times k_r e^{-0.5 \times T_a \times B_r} \cos\left(T_a \sqrt{\omega_r^2 - \frac{1}{4} \times B_r^2}\right)\right].\tag{10}$$

The constant C is defined as follows:

$$C = \frac{0.5 \times B_r^2 \times k_r}{\sqrt{\omega_r^2 - (1/4) \times B_r^2}} e^{-0.5 \times T_a \times B_r} \cos\left(T_a \times \sqrt{\omega_r^2 - \frac{1}{4} \times B_r^2}\right),\tag{11}$$

$$b_2 = 0,\tag{12}$$

$$a_0 = 1,\tag{13}$$

$$a_1 = -2 \times e^{-0.5 \times T_a \times B_r} \cos\left(T_a \times \sqrt{\omega_r^2 - 0.25 \times B_r^2}\right),\tag{14}$$

$$a_2 = e^{-T_a \times B_r},\tag{15}$$

where H_i represents the gauged current gain, R_0 and L_o represent the inverter's line resistance and inductor, ζ represents the damping factor, B_r is the resonance bandwidth, ω_r is the resonance frequency, T_a represents sampling interval, k_r is the resonance control parameter, and V_{dc} is indeed the inverter's DC input voltage.

In both modes of operation, the voltage and current of the inverter (V_I and I_I) serve as input signals. In addition, in grid-tied mode, both the solar current I_s and the battery state of charge (SOC) are utilized to create reference currents. The reference current is considered to be −10 for $I_s < 0.5$ and SOC < 10 and 2 for $I_s > 0.5$ and SOC > 10. These currents are

transformed from ab-frame to dq-frame utilizing ab-to-dq transformations. Comparing the dq-frame currents to the measured ones yields the error signals for the PR current controllers. Finally, the output control signals are transformed to ab-frame.

$$V_d = \left(I_{\mathrm{dref}} - I_d\right) \times k_{\mathrm{Pc}} + \left(I_{\mathrm{dref}} - I_d\right) \times k_{\mathrm{Rc}} \times G_R(z),$$
$$V_q = \left(I_{\mathrm{qref}} - I_q\right) \times k_{\mathrm{Pc}} + \left(I_{\mathrm{qref}} - I_q\right) \times k_{\mathrm{Rc}} \times G_R(z),$$
(16)

where I_d, I_q, I_{dref}, and I_{qref} are the measured and reference inverter output current in dq-frame. k_{Pc} and k_{Rc} are the proportional and resonant gains of the PR current controller. V_d and V_q are the measured inverter output voltage in dq-frame.

In the islanded mode, the inverter voltage is transformed to a dq-frame and compared to the self-generated 50 Hz reference voltage to generate error signals. The error signals are then applied to outer voltage controllers in order to generate dq-frame reference current signals. These reference signals are compared to the measured inverter current to produce the inner current controller's error signal. The final output signal is utilized to create the PWM signal needed to switch the inverter.

$$I_{\mathrm{dref}} = \left(V_{\mathrm{dref}} - V_d\right) \times k_{\mathrm{Pv}} + \left(V_{\mathrm{dref}} - V_d\right) \times k_{\mathrm{Rv}} \times G_R(z),$$
$$I_{\mathrm{qref}} = \left(V_{\mathrm{qref}} - V_q\right) \times k_{\mathrm{Pv}} + \left(V_{\mathrm{qref}} - V_q\right) \times k_{\mathrm{Rv}} \times G_R(z).$$
(17)

The PR current controller's proportional and resonant gains are denoted by k_{Pv} and k_{Rv}, respectively. The reference inverter output voltages in dq-frame are denoted by V_{dref} and V_{qref}.

The parameters for the adopted inverters' controls are shown in Table 3. Table 4 displays the resonant filter coefficients for both the voltage and current PR controllers. It should be noted that the limitations of the control strategy are that the coefficients of the IIR filter to implement the PR controller are sensitive, as shown in Table 4, which requires high-speed processor specifications to process them to produce the desired response. Also, the disturbance in the control loop that generates reference current may have an impact on the grid-connected current quality.

Figure 5(a) shows the magnitude resonant filter's frequency domain with gain of 0 dB at resonance frequency (50 Hz). In this case, only the error component of 50 Hz is passed. Energy is significantly reduced for all other components. At the bottom of the same figure is a display of the frequency plane phase response of the certified filter. When the filter's poles are in phase, the resonance phase will flip by 180 degrees. The PR controller's magnitude response is illustrated in Figure 5(b) with the maximum magnitude at a frequency of 50 Hz. This controller produces zero phase around 50 Hz frequency as illustrated in the phase response shown in the same figure.

2.1.2. Proposed MPPT Method. Here, we present a new MPPT control strategy that modifies standard PO and INC techniques by applying a PSO-trained ANFIS to maximize the output of a solar PV system using a boost DC/DC converter. The ANFIS

TABLE 3: The adopted inverters' control parameters.

Parameter name	Acronym	Value
Angular bandwidth around ω_o	ω_c	$2\pi 3$
Nominal AC frequency	$\omega_r = \omega_o$	$2\pi 50$
Proportional gain of PR current controllers	k_{Pc}	27
Resonant gain of PR current controllers	k_{Rc}	3
PR current/power compensators' damping coefficient	ζ	0.95
Proportional gain of PR voltage controllers	k_{Pv}	0.5
Resonant gain of PR voltage controllers	k_{Rv}	0.001
DG1 and DG2 signal gain measured	H_i	1

TABLE 4: Voltage and current PR resonant filter coefficients.

Parameter name	Value
b_0	$1.146039290275440e-04$
b_1	0
b_2	$-1.146039290275440e-04$
a_0	1
a_1	-1.999976025486589
a_2	0.999976124181453

transforms inputs into outputs using fuzzy logic and weighted ANN. The ANFIS is a technique for machine learning that takes the best features of two different approaches (backpropagation and least-square error algorithms) and combines them. Using two rules of fuzzy IF-THEN, a first-order Sugeno model is utilized to show the ANFIS structure [56]:

$$R1: \text{If } x \text{ is } A_1 \text{ and } y \text{ is } B_1, \quad \text{then } f_1 = r_1 x + p_1 y + k_1,$$
$$R2: \text{If } x \text{ is } A_2 \text{ and } y \text{ is } B_2, \quad \text{then } f_2 = r_2 x + p_2 y + k_2,$$
(18)

where x and y represent the variables of input; A_i and B_i represent the variables of fuzzy system; f_i represents the fuzzy sets' outputs; and r_i, k_i, and p_i represent the ANFIS system's design parameters, which are obtained while the ANFIS system is being trained. Figure 6 demonstrates the construction of the ANFIS. ANFIS has five-layer architecture. Each layer is explained in further detail as follows [56].

(1) Layer 1. The inputs' fuzzy membership classes are calculated using equations (19) and (20), and the resulting classifications are shown on the layer as outputs. The outputs of Layer 1 are translated from the fuzzy input membership grades [56].

$$\mathrm{Out}_{1,i} = \mu_{\mathrm{Ai}}(x), \quad i = 1, 2, \tag{19}$$

$$\mathrm{Out}_{1,i} = \mu_{\mathrm{Bi-2}}(y), \quad i = 3, 4. \tag{20}$$

The i-th node takes in x and y and is labeled A_i and B_i as inputs, which mean "low" or "high," are connected to its functions. Both $\mu_{\mathrm{Ai}}(x)$ and $\mu_{\mathrm{Bi-2}}(y)$ are free to adopt any fuzzy membership functions. Consider the following expression for $\mu_{\mathrm{Ai}}(x)$ in the context of the Gaussian membership function [56].

$$\mu_{\mathrm{Ai}}(x) = e^{\left[-0.5\left|x - \mathrm{cn}_i / d_i\right|^{g_i}\right]}. \tag{21}$$
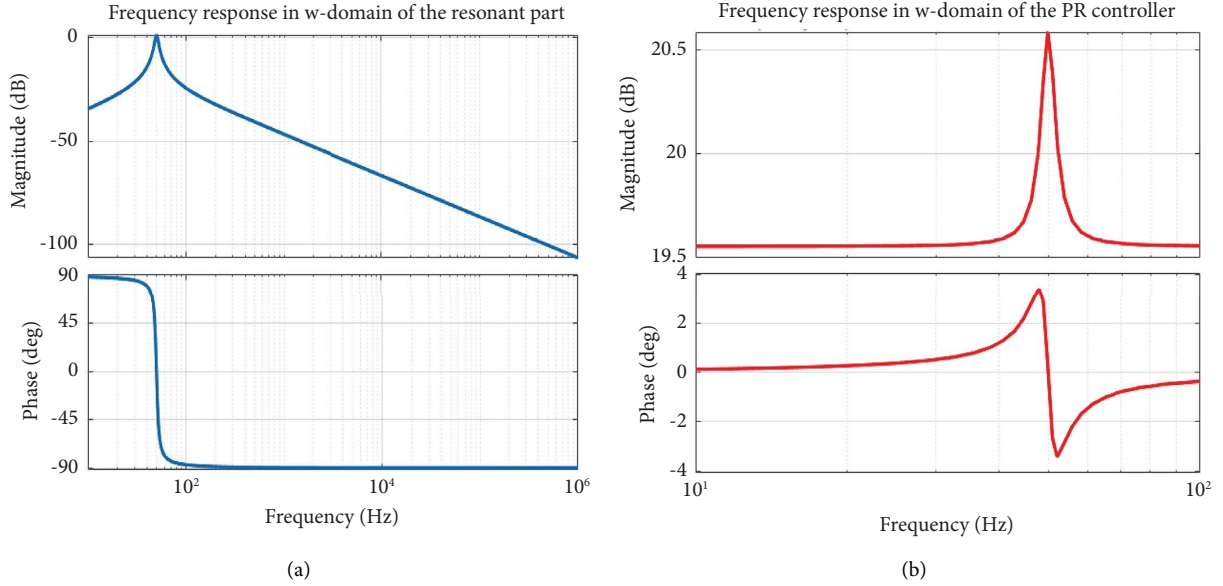
FIGURE 5: The (a) resonance filter and (b) PR controller's magnitude and phase responses.
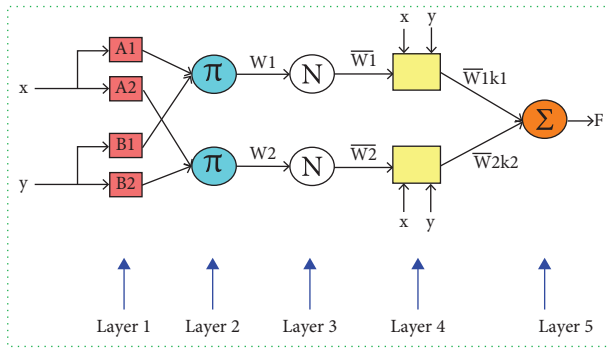

FIGURE 6: The ANFIS's architectural design.

Here, cn_i represents the center, d_i represents the breadth, and g_i represents the fuzzy factor.

(2) Layer 2. The nodes of Layer 2 are fixed nodes. The layer fuzzy tests the inputs using the AND operator and fuzzy operators. They are denoted by the character π, indicating that they perform the basic multiplier's function. The following may be used to represent this layer's output:

$$\text{Out}_{2,i} = W_i = \mu_{Ai}(x) \cdot \mu_{Bi}(y). \quad (22)$$

This is the so-called "firing strength" of the rules.

(3) Layer 3. The N-labeled fixed nodes play a part in the third logical layer. The layer's output can be expressed using the following equation (23) [56]:

$$\text{Out}_{3,i} = \overline{W_i} = \frac{W_i}{(W_1 + W_2)} \quad i = 1, 2. \quad (23)$$

(4) Layer 4. Adaptable nodes exist in layer 4. The output of a node is a first-order polynomial time its normalized firing strength. The output of this layer may be stated as follows:

$$\text{Out}_{4,i} = \overline{W_i} f_i = \overline{W_i}(r_i x + p_i y + k_i) \quad i = 1, 2, \quad (24)$$

where $\overline{W_i}$ is the layer 3 output and r_i, k_i, and p_i are the resulting parameters.

(5) Layer 5. Layer 5 has one fixed node named $\sum x$. This node compiles the data from all incoming signals. This represents the overall model's output [56].

$$\text{Out}_{5,i} = \sum_i \overline{W_i} f_i = \frac{\sum_i W_i f_i}{\sum_i W_i}. \quad (25)$$

Today's designers are tasked with keeping up with the ever-evolving ANFIS specifications and providing necessary training. When compared to gradient updates, PSO updates are more easier and faster to implement. Each particle k in the swarm has a location vector $X^k = (x^{k1}, x^{k2}, \ldots, x^{kD})$ and a velocity vector $V^k = (v^{k1}, v^{k2}, \ldots, v^{kD})$ in the D-dimensional space of study. $P^k = (p^{k1}, p^{k2}, \ldots, p^{kD})$ represents the best point in memory that this particle has visited so far. $P^z = (p^{z1}, p^{z2}, \ldots, p^{zD})$ is the optimal location reached by the swarm's particles. At each iteration, n, the location and velocity vectors are determined by the following equations:

$$v_{n+1}^{kj} = \chi \Big[c_1 \times r_{1n}^{ij} \times \big(p_n^{kj} - x_n^{kj}\big) + c_2 \times r_{2n}^{ij}$$
$$\times \big(p_n^{zj} - x_n^{kj}\big) + v_n^{kj} \Big], j \in [1, 2, \cdots, D], \quad (26)$$
$$x_{n+1}^{kj} = v_{n+1}^{kj} + x_n^{kj}, j \in [1, 2, \ldots D],$$

where c_1 and c_2 are positive constant (individual and global) learning rates, while r_1 and r_2 are random values between 0 and 1. χ is known as the constriction factor and has the following definition [51]:

$$\chi = \frac{2}{\left| -\sqrt{c^2 - 4c} + 2 - c \right|}, c = c_1 + c_2. \quad (27)$$

An all-inclusive diagrammatic representation of an ANFIS-based MPPT controller trained using a PSO is illustrated in Figure 7. Before performing error reduction, a cutting-edge hybrid ANFIS approach collects fuzzy data by modifying membership values according to learning criteria. When the proper membership settings are applied, the trained system may function as a hybrid MPPT controller. As shown in Figure 5, we can defuzzify the system and get at an output using the weighted average method by adjusting the ANFIS settings (Table 5) and the PSO settings (Table 6). The preceding and subsequent parameters have each been simulated separately. By comparison, our hybrid ANFIS--PSO method concurrently trains all parameters while minimizing the mean square error. The conventional PO and INC methods are detailed in [26]. The output signals of the PSO-based ANFIS and PO or INC techniques are averaged to obtain the final trigger signal for the boost DC/DC converter's MOSFET switch using the following equations:

$$\text{Out}_{\text{PO,MPPT}} = \frac{\text{Out}_{\text{PO}} + \text{Out}_{\text{ANFIS}}}{2}, \tag{28}$$

$$\text{Out}_{\text{INC,MPPT}} = \frac{\text{Out}_{\text{INC}} + \text{Out}_{\text{ANFIS}}}{2}. \tag{29}$$

2.1.3. ESS Control Method-Based Buck-Boost Converter.
The adopted DC-DC converter's circuit schematic for ESS is demonstrated in Figure 3. It is a bidirectional buck-boost design. This converter connects ESS to the DC bus. Depending on the operational state, boost and buck modes can be configured. The converter functions using two controllable switches (S1 and S2), whose functioning is complimentary, implying that while one is active, another has to be in the off state. Based on the maximum duty ratio, the converter operates in boost mode if S1 is activated and in buck mode if S2 is activated [57]. An input inductor (L) delivers a nonpulsating current and enables transfer of power from the source to the DC load. The controller must ensure that the switches are not turned on at the same time, since this would result in a harmful current flowing through the very small parasitic resistance created between the ground and the input [57]. During a certain amount of time,

both switches have to remain in the off state [57]. The converter's components can be constructed when the DC-DC converter operates in the boost continuous conduction mode (CCM) using the calculations provided by [58]. The duty cycle at minimal input voltage is calculated by equation (30) when converter efficiency is estimated at 95%:

$$D = \frac{V_2 - V_1 \times \eta}{V_2} = \frac{400 - 240 \times 0.95}{400} = 0.43, \tag{30}$$

where V_1 and V_2 are the converter's output and input voltages, respectively, and η is the converter efficiency.

For estimating inductor ripple current (ΔI), assuming inductor ripple current equals 10% of the output current:

$$\Delta I = \frac{0.1 \times I_{2,\max} \times V_2}{V_1} = \frac{0.1 \times 5 \times 400}{240} = 0.083A, \tag{31}$$

where $I_{2,\max}$ represents the maximum output current.

The inductor value (L) is given by

$$L = \frac{V_1 \times (V_2 - V_1)}{\Delta I \times f_s \times V_2} = \frac{240 \times (400 - 240)}{0.083 \times 10 \times 10^3 \times 400} = 0.115H, \tag{32}$$

where f_s is the switching frequency.

Next, the minimal output capacitance (C_{out}) assuming 1% output voltage fluctuation (ΔV_2) is calculated as follows:

$$C_{\text{out}} = \frac{I_{2,\max} \times D}{\Delta V_2 \times f_s} = \frac{5 \times 0.43}{(0.01 \times 400) \times 10 \times 10^3} = 5 \times 10^{-5} f. \tag{33}$$

Note that the above equations (30)–(33) are used to design adopted boost converters (e.g., for solar PV and wind turbines). Using the aforementioned formulae [58], while the converter operates in the buck CCM, the higher duty cycle with a predicted 95% efficiency may be calculated:

$$D = \frac{V_1}{V_2 \times \eta} = \frac{240}{400 \times 0.95} = 0.63. \tag{34}$$

Afterward, the buck CCM's minimum input capacitance (C_{in}) is determined, which is based on an estimate of a 1% change in the input voltage (ΔV_1).

$$C_{\text{in}} = \frac{V_1/\eta \times (1 - (V_1/V_2 \times \eta))}{8 \times \Delta V_1 \times f_s^2 \times L} = \frac{240/0.95 \times (1 - (240/400 \times 0.95))}{8 \times 0.01 \times (10 \times 10^3)^2 \times 0.115} = 1 \times 10^{-4} f. \tag{35}$$

The adopted ESS converter architecture utilizes a control approach based on pulse-width modulation (PWM) and a constant frequency of switching. A conventional PI controller is developed for both operational modes, with proportional gain ($k_p = 0.0001$) and integral gain ($k_i = 0.05$) achieved by trial and error. The following equations describe the switching signals:

$$S_1 = \text{PWM}\left[(V_{\text{ref}} - V_2) \times k_p + (V_{\text{ref}} - V_2) \times \frac{k_i}{S} \right] \text{ and } S_2$$

$$= \overline{S_1}, \tag{36}$$
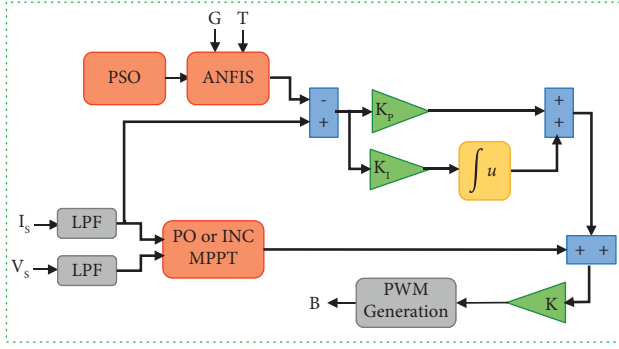
where V_{ref} is the reference DC bus voltage.

FIGURE 7: The proposed MPPT technique-based boost converter of solar PV.

TABLE 5: ANFIS parameters.

Parameter name	Value
Input number	2
Output number	1
Solar irradiance range	[1, 1000]
Temperature input range	[15, 35]
Output range	[210, 275]
Counting functions of memberships, for each input and output	10
Rule number	10

TABLE 6: PSO parameters.

Parameter name	Value
The weight of inertia	1
Damping ratio of inertia weight	0.99
Coefficient of individual learning	1
Global learning parameter	2
Maximum number of iterations	1000
Swarm size	25
Lower bound	−25
Upper bound	25

3. The DSM Formulation

3.1. Mathematical Scheduling Framework for Load Appliances.

The appliances can be classified as nonshiftable and shiftable based on their operating hours, energy usage, and the end-user's preferences. In general, time-scale-shiftable appliances may be set to any time zone. Their overall energy usage is calculated as follows:

$$E_{\text{SL}}(t) = \sum_{t=1}^{24} \sum_{m=1}^{N_{\text{SL}}} Z_{\text{SL}}(r,t) \times A_{\text{SL}}(r,t), \quad (37)$$

where time slots are represented by t, the total number of shiftable appliances by N_{SL}, $A_{\text{SL}}(r,t)$ represents the power used by an appliance r during t-time, and the ON/OFF status of a shiftable appliance during the shift's beginning (T_1) and finishing (T_2) times by Z_{SL}.

$$Z_{\text{SL}}(r,t) = \begin{cases} 1 & \text{Appliance } (r) \text{ is ON} \\ 0 & \text{Appliance } (r) \text{ is OFF} \end{cases} \forall T_1 \leq t \leq T_2. \quad (38)$$

The daily cost of consumption for shiftable appliances ($C_{\text{SL}}(t)$) is

$$C_{\text{SL}}(t) = E_{\text{SL}}(t) \times \text{Pr}(t), \quad (39)$$

where $\text{Pr}(t)$ denotes the electrical tariff price, which in this study is assumed as a real-time price that changes every time hour.

Fixed or nonshiftable appliances cannot have their load profiles changed in any way. Their daily energy demand ($E_{\text{NSL}}(t)$) is expressed as

$$E_{\text{NSL}}(t) = \sum_{t=1}^{24} \sum_{i=1}^{N_{\text{NSL}}} Z_{\text{NSL}}(u,t) \times A_{\text{NSL}}(u,t). \quad (40)$$

The ON/OFF state of each nonshiftable appliance u is represented by $Z_{\text{NSL}}(u,t)$, where N_{NSL} is the nonshiftable appliance count, u is the number of appliances, and $A_{\text{NSL}}(u,t)$ is the power usage of every nonshiftable device.

$$Z_{\text{NSL}}(u,t) = \begin{cases} 1 & \text{Appliance } (u) \text{ is ON} \\ 0 & \text{Appliance } (u) \text{ is OFF} \end{cases} \forall T_1 \leq t \leq T_2. \quad (41)$$

The daily nonshiftable appliance operating expenditures ($C_{\text{NSL}}(t)$) are as follows:

$$C_{\text{NSL}}(t) = E_{\text{NSL}}(t) \times \text{Pr}(t). \quad (42)$$

In equations (43) and (44), the total energy consumption ($E_T(t)$) and related costs ($C_T(t)$) of nonshiftable and shiftable appliances are estimated, respectively.

$$E_T(t) = E_{\text{SL}}(t) + E_{\text{NSL}}(t), \quad (43)$$

$$C_T(t) = C_{\text{SL}}(t) + C_{\text{NSL}}(t). \quad (44)$$

3.2. Constraints.

After the shift procedure, the daily use of load demand should be the same as it was before scheduling [1].

$$\sum_{t=1}^{24} \sum_{m=1}^{N_{\text{SL}}} B(m,t) = \sum_{t=1}^{24} \sum_{m=1}^{N_{\text{SL}}} A(m,t), \quad (45)$$

where ($A(m,t)$) represents the daily load demand usage after scheduling has occurred, and $B(m,t)$ represents the daily load use before scheduling has occurred.

According to equation (46), at time step t, there should be less shifted-load than shiftable appliances.

$$\sum_{t=1}^{24} H(t) \geq \sum_{t=1}^{24} S(t). \quad (46)$$

The shifted appliances' power is represented by $S(t)$ and for the shiftable appliances by the letter $H(t)$.

3.3. Optimization Algorithms.

Here are three DSM meta-heuristic optimization methods. These algorithms apply to a typical building with nine appliances (three nonshiftable and six shiftable). The adopted load appliances' information is described in Table 7. Our goal is to establish power usage scheduling. Many academics have proposed residential DSM optimization solutions. To optimize electricity use, we provided SSA, BSOA, and CSO optimization approaches. SSA is based on sparrows' foraging and predator avoidance. The orientation game underpins the BSOA's game-theoretic optimizer. The referee directs BSOA's orientation game's searcher agents around the playground. The CSO optimizes cockroach swarm foraging behavior. These algorithms compare energy use with the unplanned load profile to transfer shiftable equipment from peak to off-peak hours. The mathematical models of the adopted algorithms are described as follows.

3.3.1. Sparrow Search Algorithm.

In 2020, Xue and Shen introduced the sparrow search algorithm [59]. Avoiding predators and feeding sparrows are the basis of the SSA. It replicates the sparrow team foraging: finders (discoverers) and followers. A segment of the populace undertakes reconnaissance and early warning simultaneously. They'll avoid food if threatened. The matrix below shows sparrow positions [59]:

$$Z = \begin{bmatrix} z_{1,1} & z_{1,2} & \cdots & z_{1,d} \\ z_{2,1} & z_{2,2} & \cdots & z_{2,d} \\ \vdots & \vdots & \vdots & \vdots \\ z_{n,1} & z_{n,2} & \cdots & z_{n,d} \end{bmatrix}, \quad (47)$$

where n is the sparrow count and d is the variable's dimension. Then, the fitness vector for all sparrows is [59]

$$F(Z) = \begin{bmatrix} f\left(\begin{bmatrix} z_{1,1} & z_{1,2} & \cdots & z_{1,d} \end{bmatrix}\right) \\ f\left(\begin{bmatrix} z_{2,1} & z_{2,2} & \cdots & z_{2,d} \end{bmatrix}\right) \\ \vdots & \vdots & \vdots & \vdots \\ f\left(\begin{bmatrix} z_{n,1} & z_{n,2} & \cdots & z_{n,d} \end{bmatrix}\right) \end{bmatrix}, \quad (48)$$

where $F(Z)$ is the sparrows' fitness, and each row is its fitness. The discoverers must find food and help the populace get fitter while prioritizing food acquisition. Thus, the discoverers may find food in a far greater region than the competitors. If a sparrow detects a predator, it sings to warn others. If the warning value is greater than the safe one, the finder will lead the group to safer foraging places. Each iteration's sparrow finder location is [59]

$$Z_{i,j}^{k+1} = \begin{cases} Z_{i,j}^k \times e^{-(i/\alpha.\text{iter}_{\max})} & \text{for } R < \text{ST}, \\ Z_{i,j}^k + Q \times L & \text{for } R \geq \text{ST}, \end{cases} \quad (49)$$

where $Z_{i,j}^k$ is the current position of the sparrow finder, k denotes the recent iteration, $j = 1,2,...,d$ is the i-th sparrow's size at this iteration, $\text{iter}_{\max}$ is the highest number of iterations

allowed, $\alpha \in (0, 1]$ is a random integer, $\text{ST} \in [0.5, 1]$ and $R \in [0, 1]$ are the alarm and safety limits, Q is a normal-distributed random integer, and L is 1 if and only if every dimensioned matrix element is 1. When $R < \text{ST}$, the finder starts a comprehensive search; when $R > \text{ST}$, predators have attacked several sparrows, and all sparrows must evacuate immediately.

Low-energy individuals have a lower chance to participate in group foraging. Hungry immigrants may escape for energy. Since the finder may forage nearby, entrants may always look for them. Some participants can watch the finders for food competition and predation. If the finder leaves to compete for food, some participants pay closer attention. If they succeed, they will get the finder's meal immediately. The following formula updates enrollee positions [59]:

$$Z_{i,j}^{k+1} = \begin{cases} Q \times e^{-\left(Z_{\text{worst}}^k - Z_{i,j}^k/i^2\right)} & \text{for } i > \left(\dfrac{n}{2}\right), \\ Z_p^{k+1} + \left| Z_{i,j}^k - Z_p^{k+1} \right| \times A^+ \times L & \text{Otherwise}, \end{cases} \quad (50)$$

where Z_{worst}^k is the current search space's worst position, Z_p^k represents the occupied optimal position, A^+ is a random factor of size d with entries randomly distributed between [1, 1], and $A^+ = A^T (AA^T)^{-1}$. If i exceeds $n/2$, the i-th entrant is least fit and most likely to die. 10%–20% of sparrows are hazard alert, which randomly generates their beginning placements. Sparrows at the group's perimeter will quickly fly to the secure region to locate a better location. To discover other sparrows, the sparrows in the center will move around randomly. Scout's math model [59] is

$$Z_{i,j}^{k+1} = \begin{cases} Z_{\text{best}}^k + \beta \times \left| Z_{i,j}^k - Z_{\text{best}}^k \right| & \text{for } f_i > f_g, \\ Z_{i,j}^k + K \times \left(\dfrac{\left| Z_{i,j}^k - Z_{\text{worse}}^k \right|}{(f_i - f_w) + \varepsilon} \right) & \text{for } f_i = f_g, \end{cases} \quad (51)$$

where Z_{best}^k is the current best global position, β is the step size control parameter in the format of a random number normally distributed with a mean of zero and a variance of one, and K is a random sparrow movement between −1 and 1. f is the optimization problem's fitness function, f_i, f_g, and f_w are the world's current, optimum, and worst levels for sparrow fitness; ε represents the lowest constant needed to avoid a zero division mistake. For simplicity, $f_i > f_g$ means sparrows are near the group's edge, Z_{best}^k around the center; otherwise, $f_i = f_g$ means sparrows in the middle realize there is a danger to their species.

The DSM control approach uses SSA to regulate power consumption depending on the discoverer's position and shiftable loads' locations. This program manipulates energy consumption's both horizontal and vertical axes. Energy consumption is described by the vertical axis and time by the horizontal. By comparing the greatest possible energy consumption with the maximum possible time slot parameters, this algorithm finds the optimal consumption

TABLE 7: The adopted nonshiftable and shiftable load appliances' information.

Load type	Appliances	Operating time	Rated power (kW)
Shiftable load	Microwave oven	7–9, 11–14, 18–22, 31–33, 35–38, 42–46	0.75
	Washing machine	7–12, 15–20, 31–36, 37–44	0.13
	Water heater	1–10, 15–24, 25–34, 37–48	0.65
	Dish washer	7–9, 11–14, 18–22, 31–33, 35–38, 42–46	0.2
	Coffee maker	8–18, 32–42	0.13
	Vacuum cleaner	10–15, 18–22, 34–39, 42–46	0.2
Nonshiftable load	Air conditioning	All time	1.75
	Electric vehicle	All time	0.65
	Water pump	All time	0.455

pattern that minimizes the total cost of electricity use. Equation (44) shows the goal function to be minimized.

3.3.2. Binary Orientation Search Algorithm. In 2019, BOSA was presented [49]. BSOA emulates orientation games. The referee directs participants in this game. Equation (52) shows the players' starting positions [49]

$$Z_i = \left(z_i^1, \cdots, z_i^d, \cdots, z_i^n \right). \tag{52}$$

The i-th player's location in dimension d is denoted by the variable z_i^d, and n is the total variables' number.

$$q_i = \frac{0.8T + 0.2k}{T}, \tag{54}$$

$$\text{Orientation}_i^d = \begin{cases} \text{sign}\left(\text{Referee}^d - \text{Player}_i^d\right) & \text{for} \quad \text{rand} < q_i \\ -\text{sign}\left(\text{Referee}^d - \text{Player}_i^d\right) & \text{otherwise,} \end{cases} \tag{55}$$

where T denotes the maximum iteration and k is the iteration number.

However, despite the need that all players advance toward the referee, some of them may be unable to do so. Equations (56) and (57) are used to mimic this issue [49].

$$\text{error} = 0.2\left(\frac{T - k}{T}\right), \tag{56}$$

$$z_i^d = \begin{cases} z_i^d + \text{rand} \times \text{Orientation}_i^d \times z_h^d, \\ z_l^d + \text{rand} \times \left(z_h^d - z_l^d\right), \end{cases} \tag{57}$$

where z_h^d and z_l^d are the maximum and minimum limits, respectively.

The referee is determined by which player has the best fitness function value for each iteration, as seen in the following:

$$\text{Referee} = \begin{cases} \text{Maximization problem: location of} \quad \max \ (f), \\ \text{Minimization problem: location of} \quad \min \ (f). \end{cases} \tag{53}$$

The fitness function's value is denoted by (f).

The hand of a referee may or may not be going in the same direction as the referee's body. In contrast, players need just pay attention to the referee's hand. Two equations, (54) and (55), are utilized to model the direction [49]:

The location of the particle in discrete space is indicated by the integers 0 and 1. A shift from zero to one, or one to zero, represents motion for an agent in any dimension. Due to this, the player's position is updated based on a probability function that takes into account the displacement in each dimension. The interval [0 1] is selected to limit the probability function $dZ^{j,d}$ in BOSA. The probability function is denoted by the following equation [49]:

$$S\left(dZ^{j,d}(k)\right) = \left|\tanh\left(dZ^{j,d}(k)\right)\right|. \tag{58}$$

Equation (59) is used to simulate each player's new location depending on the probability function [49].

$$Z^{j,d}(k+1) = \begin{cases} \text{complement}\left(Z^{j,d}(k)\right) & \text{for rand} < S\left(dZ^{j,d}(k)\right), \\ Z^{j,d}(t) & \text{Otherwise.} \end{cases} \tag{59}$$

In order to solve the problem being studied, the following steps outline how to implement the suggested optimum DSM program based on BSOA, taking into consideration players' locations which are determined by the schedule of controllable loads. This algorithm determines the most cost-effective schedule for using energy, given
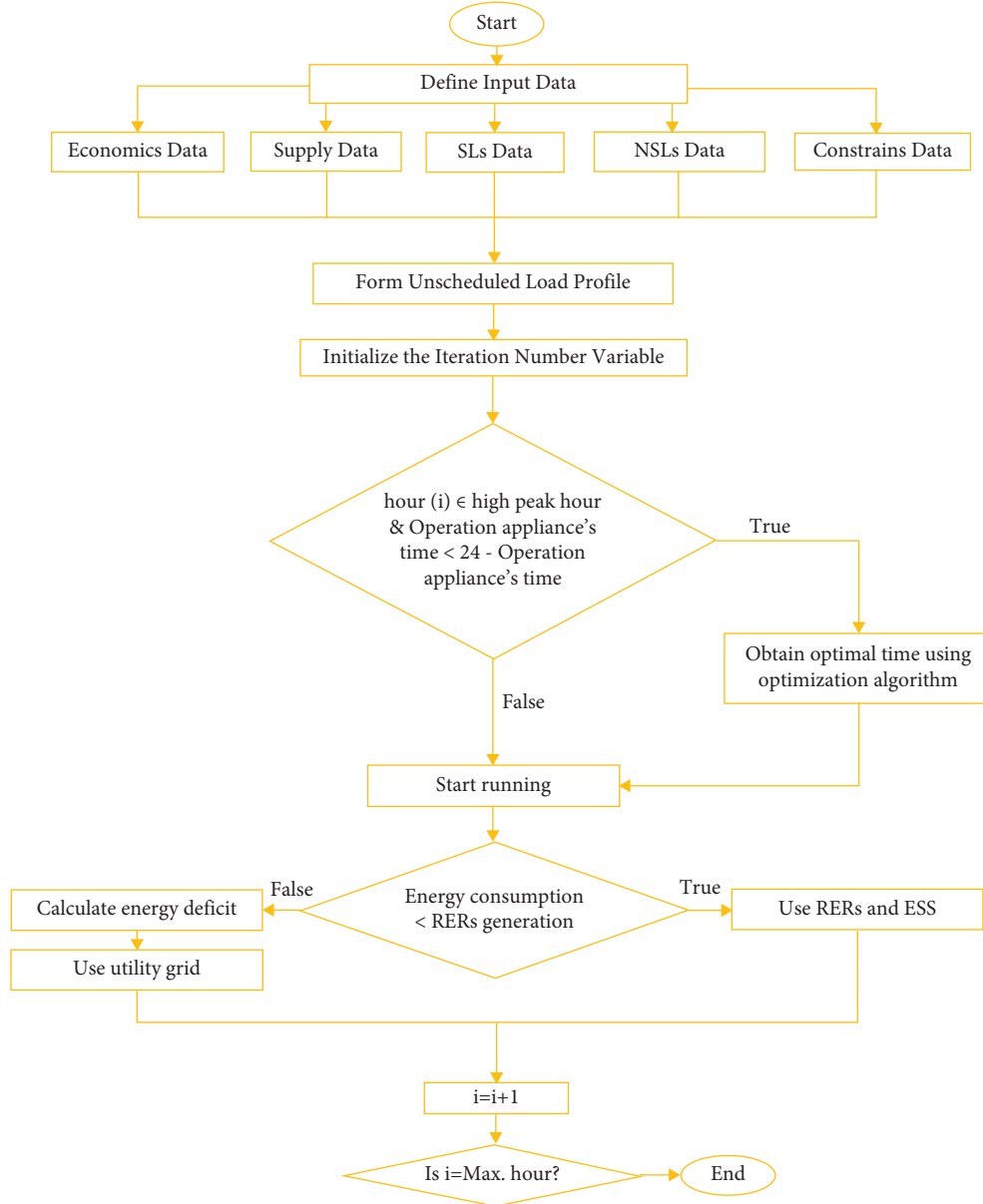
FIGURE 8: DSM-based demand management flowchart.

a maximum amount of energy and a maximum number of available time slots.

3.3.3. Cockroach Swarm Optimization (CSO) Algorithm.

Cockroaches' foraging behavior—swarming, dispersing, and avoiding light—creates CSO [60, 61]. Thus, the CSOA follows cockroach rules. The algorithm generates possible solutions first. The search area generates random initial solutions. Each iteration, the CSO algorithm uses dispersal, merciless conduct, and chase-swarming to solve optimization problems. In the chase-swarming process, the strongest cockroaches find the optimal local solutions (P_i), form tiny swarms, and move toward the optimal solution in the following cycle (P_g). Within its visible range, each individual (X_i) in this technique obtains its local optimum. A stronger

cockroach in a tiny group may discover a better solution because individuals seek their local optimums differently. From their local optimum, cockroaches seek the best global solution [62]. The dispersal of individuals is another process. To preserve cockroach variety, it is done periodically. Each cockroach moves in the search area at random. In the absence of food, weaker cockroaches are eaten [62]. CSOA model [63, 64] is as follows:

(1) Chase-Swarming Behavior:

$$Z_i = \begin{cases} Z_i + \text{steprand.} \left(P_i - Z_i \right) & P_i \neq Z_i \\ Z_i + \text{step.rand.} \left(P_g - Z_i \right) & P_i = Z_i, \end{cases} \quad (60)$$

where Z_i is the cockroach position, step is a constant, rand is a random integer between 0 and 1, p_i is the
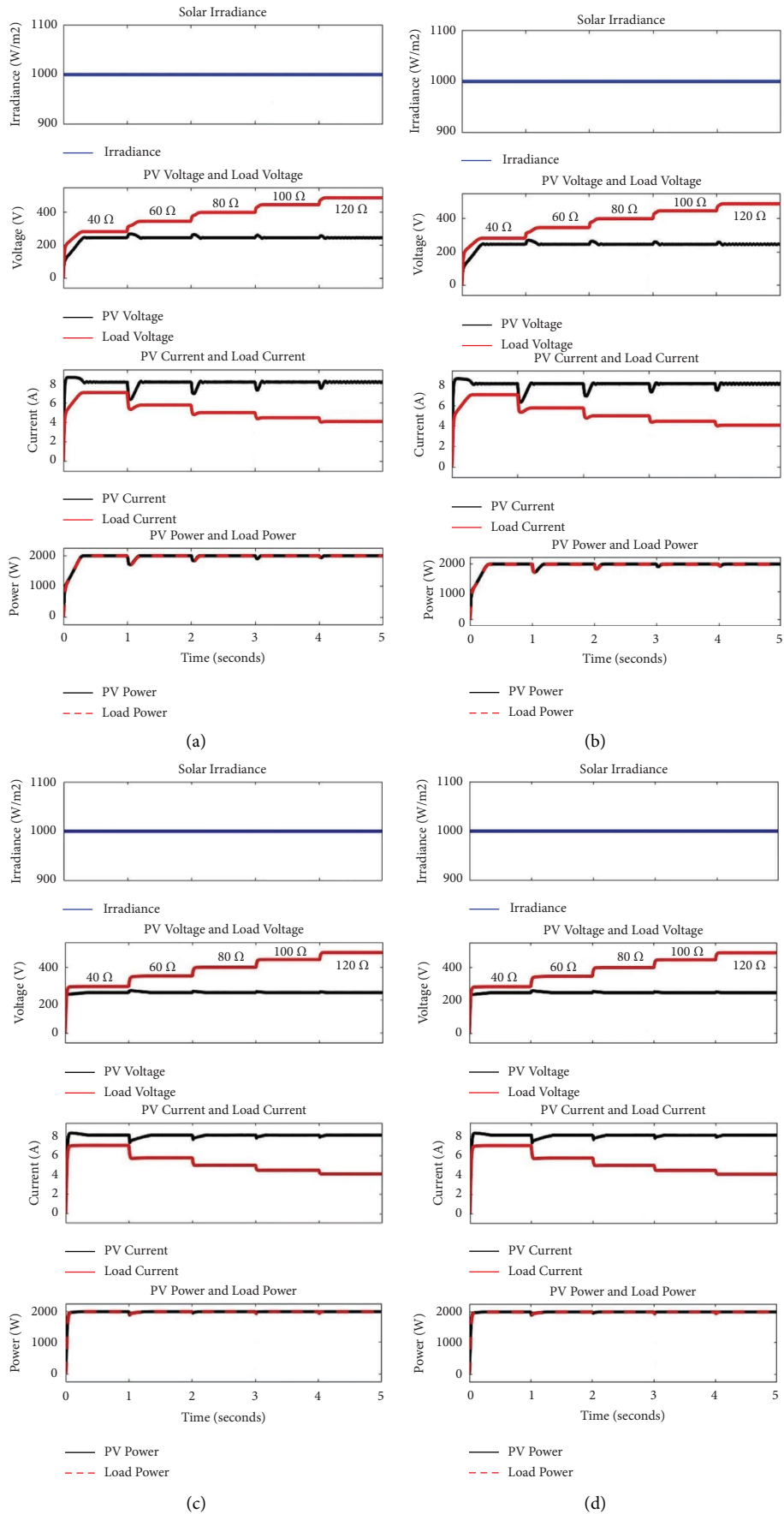
Figure 9: The solar PV and load responses under load resistance variations.
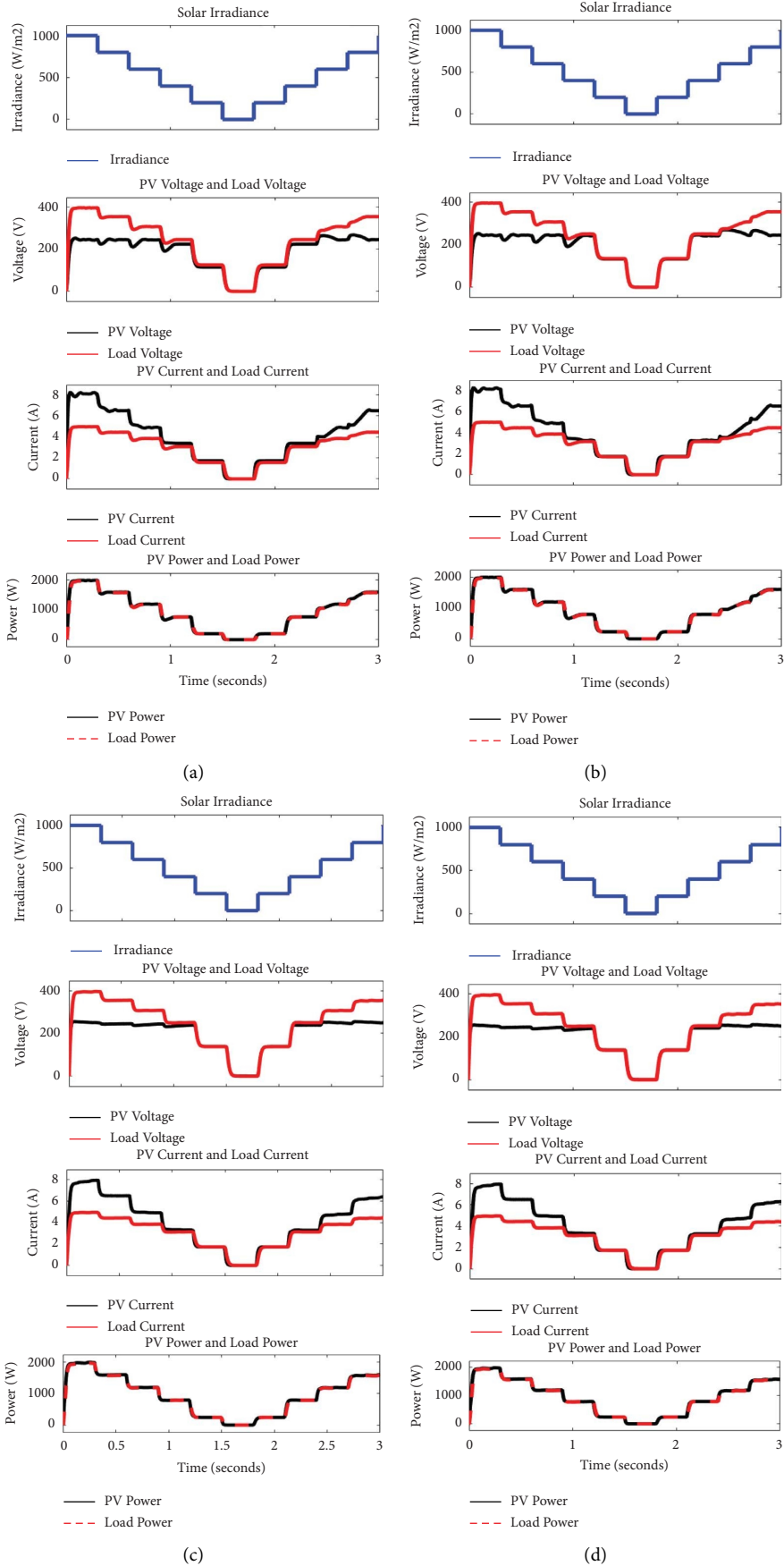
FIGURE 10: The solar PV and load responses under solar irradiance variations.
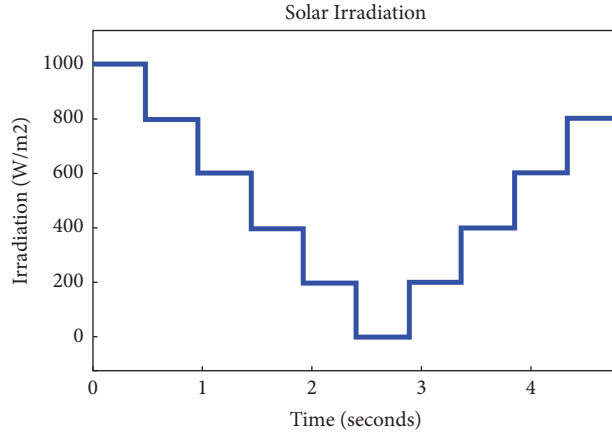
FIGURE 11: The adopted solar radiation in test 2.
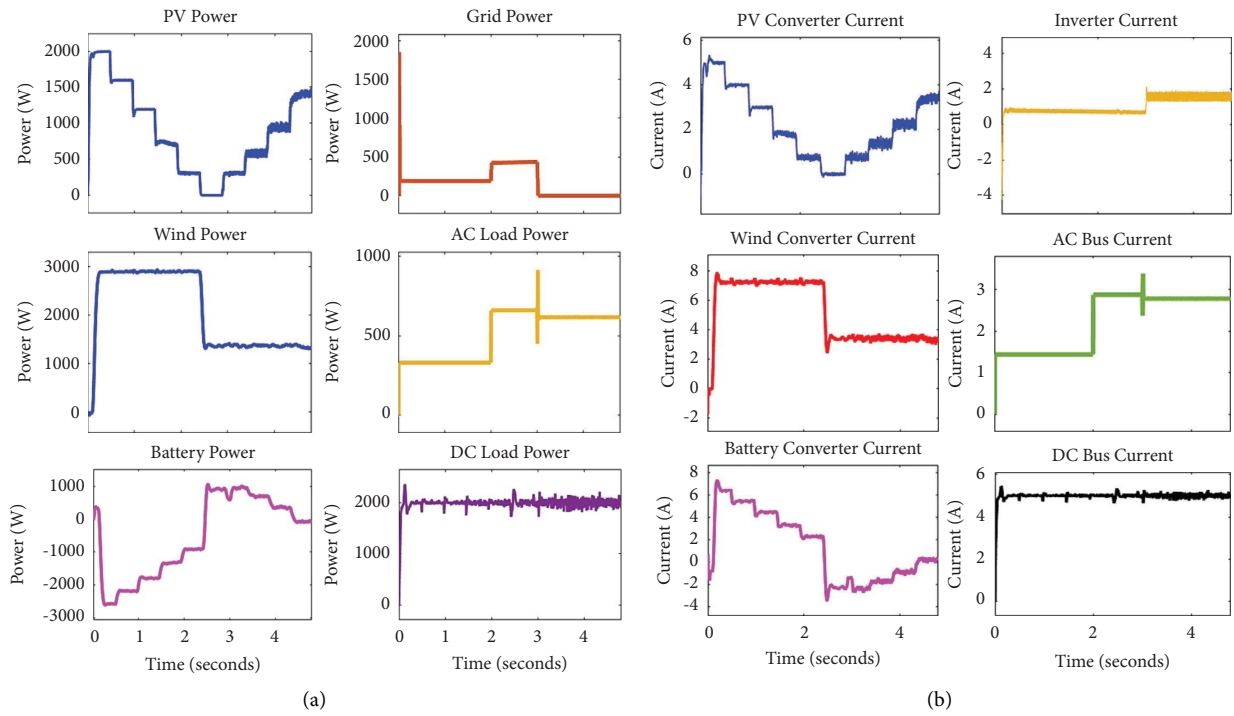
FIGURE 12: (a) Powers of the generation units and loads and (b) generation units and load currents.

individual's perfect position, and P_g is the global optimum position.

$$p_i = \text{Opt}_j\left\{X_j, |X_i - X| \leq v\right\}, \tag{61}$$

where $i = 1, 2, .., N$ and $j = 1, 2, .., N$, and the perceptual distance v is constant.

$$P_g = \text{Opt}_i\{Z_i\}. \tag{62}$$

(2) Dispersion Behavior:

$$Z_i = Z_i + \text{rand}(1, D), \tag{63}$$

where the D-dimensional random vector is generated using $\text{rand}(1, D)$.

(3) Ruthless Behavior:

$$Z_u = P_g, \tag{64}$$
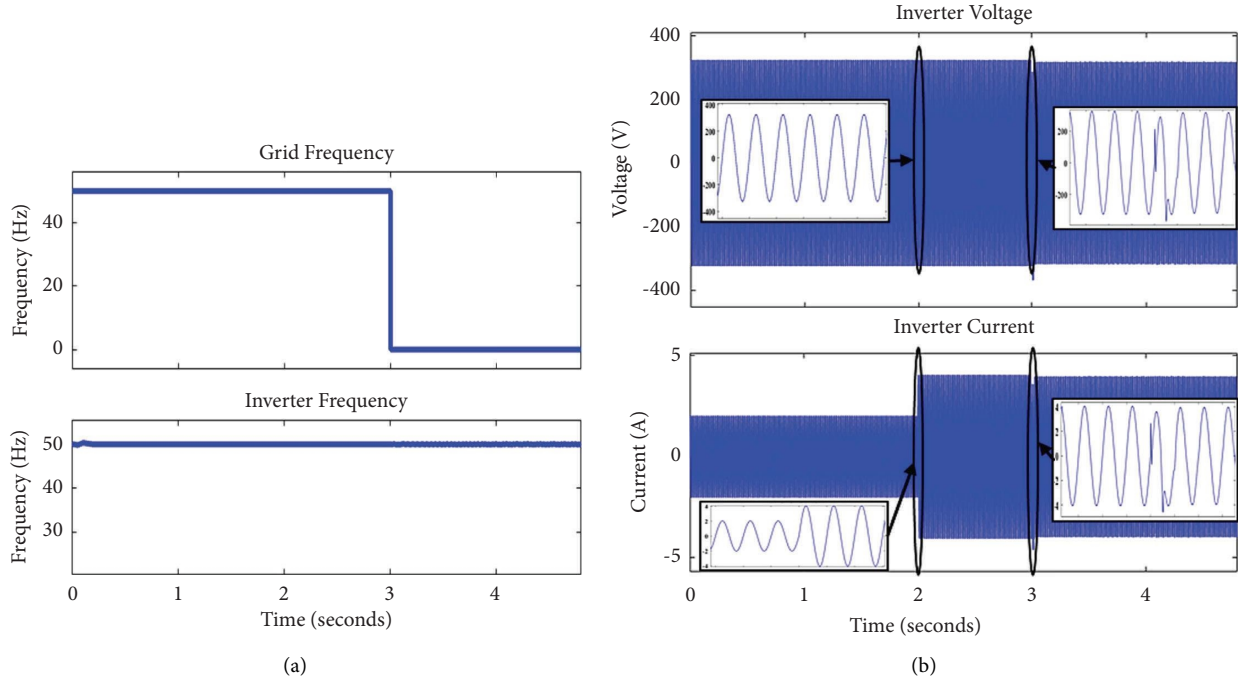
FIGURE 13: (a) Grid and inverter frequencies and (b) inverters' output voltage and current waveforms.

where u is a nonzero random number between [1; N].

This paper integrates the CSO with DSM power consumption control. This algorithm shifts energy utilization. In the consumption profile, electricity usage is vertical axis while time is horizontal. This algorithm finds the cheapest energy consumption pattern based on user-specified maximum energy usage and time slots.

As mentioned previously, appliances are usually categorized as nonshiftable and shiftable depending on energy consumption, hours of usage, and individual user preferences. Appliances with a flexible time scale may be adjusted to any off-peak time zone, allowing consumers to conserve costs via the use of optimization algorithms. Following the application of optimization-based load transferring, energy used is compared with the RERs to be provided by RERs or utilized by the utility grid to meet the energy deficiency. This process is shown in Figure 8.

4. Performance Results

Using MATLAB/Simulink, the proposed system underwent four tests to determine the performance of maximum power extraction from solar PV, islanded and grid-connected modes of operation, MG operation without and with DSM, and AC load shift in transition to island mode.

4.1. Test 1: Maximum Power Extraction from Solar PV. There have been two tests of the PV system using MPPT techniques to achieve solar PV and load responses (voltage, current, and power) under load and solar irradiance variations. As seen in Figure 9, the solar PV is subject to step load resistance variations (the load resistance is increased from $40\,\Omega$ to $60\,\Omega$ at $t = 1$ sec, to $80\,\Omega$ at 2 sec, which is the optimal value to produce 2000 W, to $100\,\Omega$ at 3 sec, and to $120\,\Omega$ at 4 sec). The applied solar irradiance is $G = 1000\,\text{W/m}^2$ and reference temperature ($T = 25^\circ\text{C}$). The PV system, as illustrated in Figure 10, has been tested in a variety of radiation conditions. It is obvious that the steady-state error is not completely eradicated by the conventional PO and INC techniques, nor are they quick to respond as shown in Figures 9(a), 9(b), 10(a), and 10(b). As can be seen in Figures 9(c), 9(d), 10(c), and 10(d), the proposed MPPT methods are capable of achieving both zero steady-state error and rapid response. Regardless of load resistance variations around the optimal value or variations in solar irradiation, the generated and load powers are maintained constant at the maximum point (2000 W).

4.2. Test 2: Islanded and Grid-Connected Modes of Operation. In test 2, MG operates initially in grid-tied mode. At 2 sec time point, the AC load is increased from 350 W to 700 W. At 3 sec time point, the MG control is transitioning into the islanded mode of operation. During this scenario, the adopted solar irradiance is changed, as seen in Figure 11, and the wind speed is reduced from 12 m/sec at the time point (2.4 sec) to 10 m/sec. The production units and load powers are shown in Figure 12(a). The amount of received solar radiation is instantly related to the amount of generated power from solar PV. At a time of 2.4 sec, the wind power decreases because the wind speed drops from 12 m/sec to 10 m/sec. The battery is in charge mode when there is solar radiation and in discharge mode when solar radiation is removed. Generating power is equal to the loads; hence, the
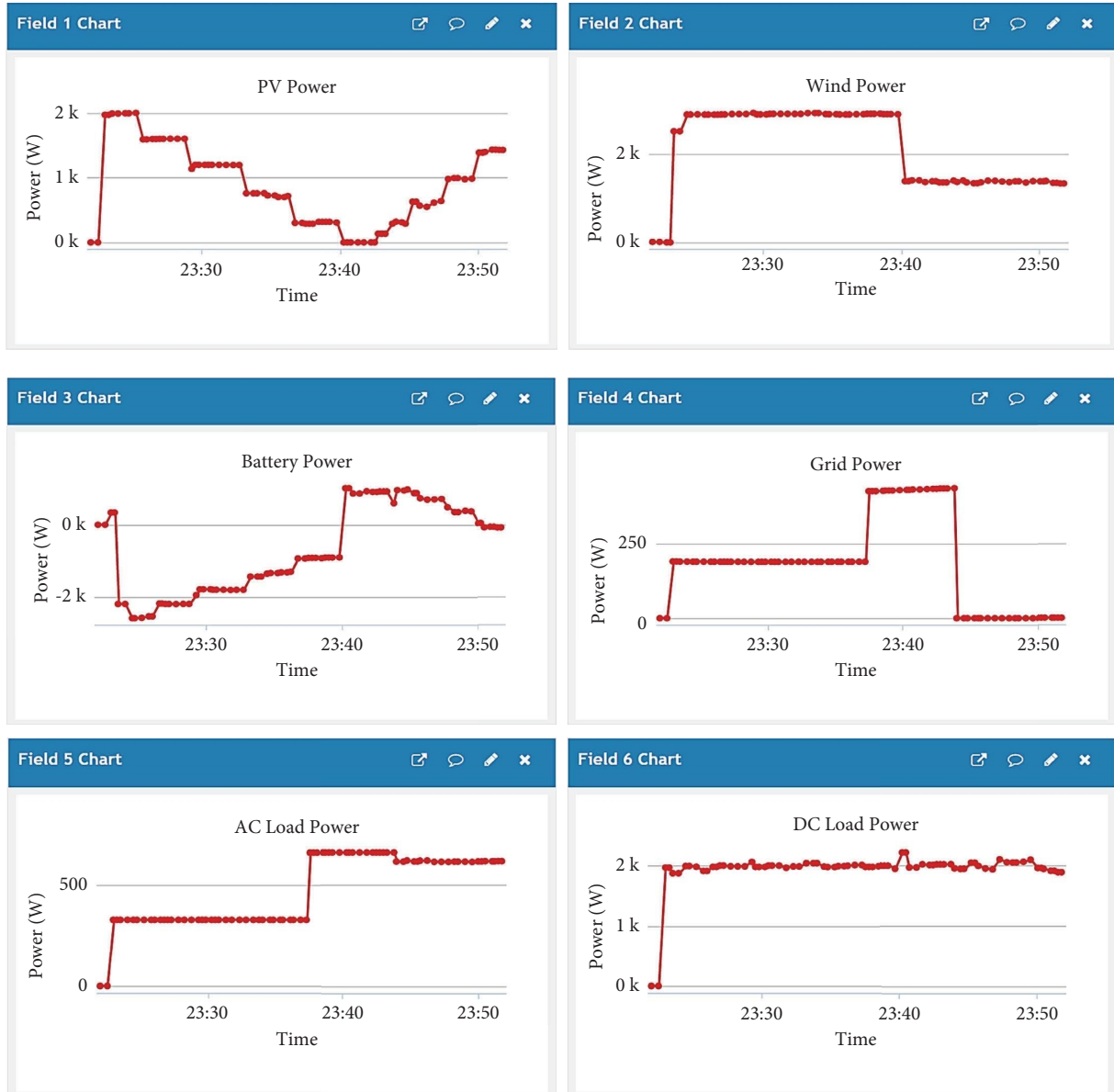
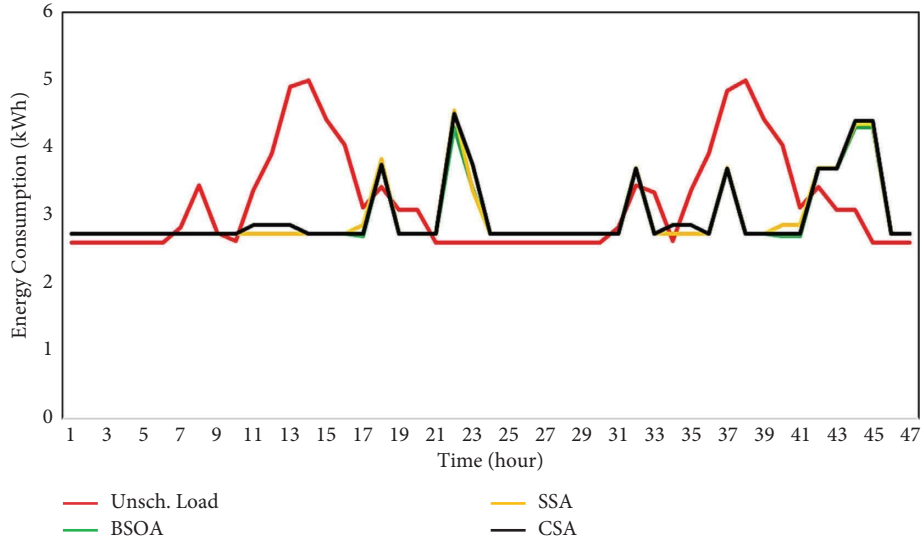FIGURE 14: The results of the system power-balanced displayed on the ThingSpeak platform in test 2.

Figure 15: Energy consumption profile with and without applying adopted algorithms-based DSM.
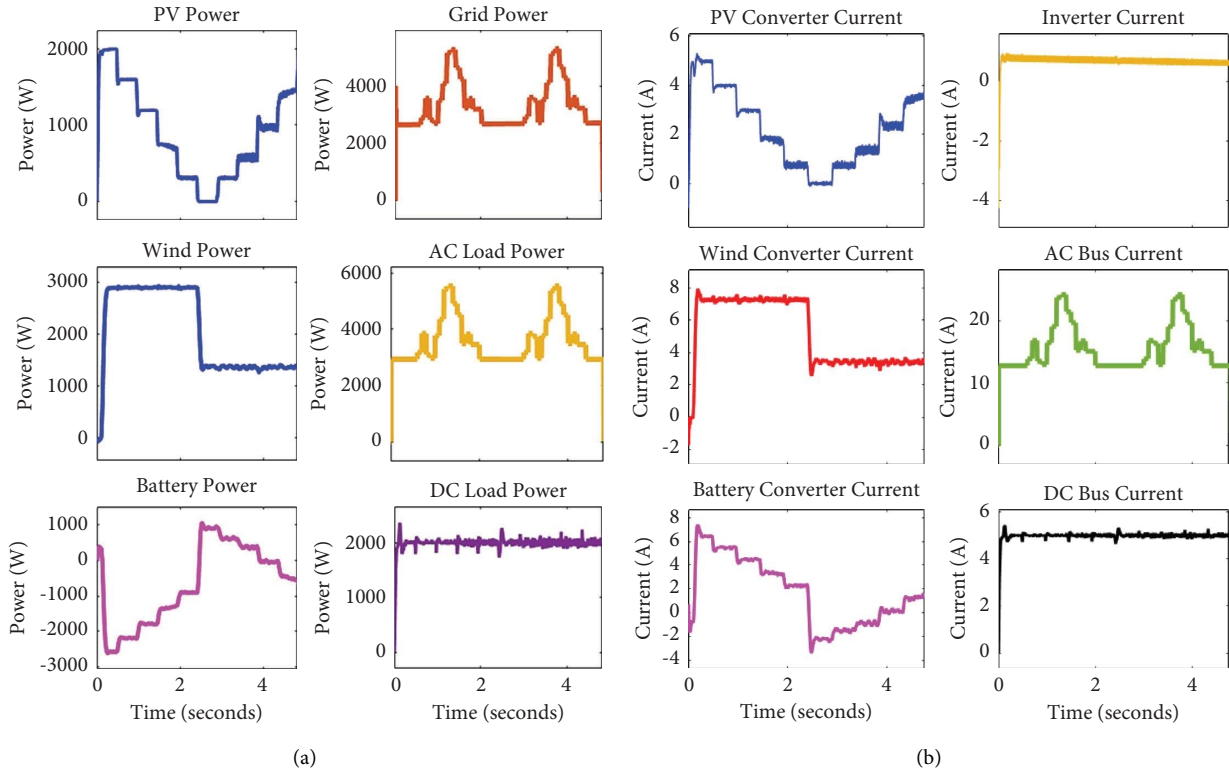

(a)

(b)

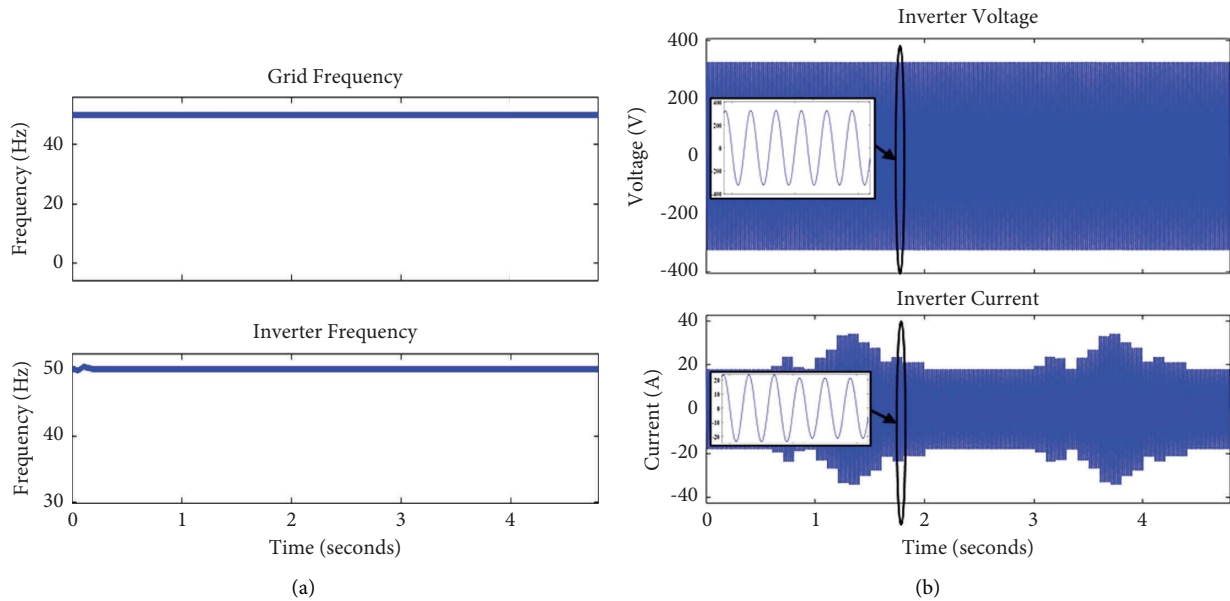Figure 16: (a) Load-generation powers and (b) load-generation unit currents without adopting DSM.

FIGURE 17: (a) Grid and inverter frequencies and (b) inverters' output voltage and current waveforms without applying DSM.

power is balanced. Figure 12(b) depicts the current flowing through each source and load. Exactly, the frequency of the grid is the output voltage signal frequency of the inverter in grid-tied mode as shown in Figure 13(a). In the islanded mode (after time point 3 sec.), it is clear that the frequency of the grid is zero (no grid-connected), and the inverter can provide 50 Hz pure sinewaves. Figure 13(b) displays the waveforms of both the inverter's current and voltage at the output terminals. The results of power-balancing are displayed using the ThingSpeak platform and EI technology, as illustrated in Figure 14.

4.3. Test 3: MG Operation without and with DSM. The system's responsiveness to the DSM program is examined in this test. The optimal DSM is developed using recent optimization methods (BSOA, SSA, and CSA). The DSM subsystem's settings (the optimization algorithms' control parameters) are selected based on a maximum time shift of 4, a population size of 30, and a total of 1000 iterations. Figure 15 illustrates the results of the load demand consumption with and without adopting the proposed algorithm-based optimum DSM. It is evident that the DSM decreases the peak of energy usage, where the peak is lowered from 5.2 kWh to 4.6 kWh. Since peak consumption has decreased, the load factor has improved (load factor = average consumption divided by peak consumption). The MG has been exposed to both unscheduled load (the red curve, which represents load demand prior to DSM application) and scheduled load demand (other curves related to adopted algorithms, which are the load profile after applying DSM). The results of power-balancing are shown in Figure 16(a) before applying DSM. Increases in the load demand profile are clearly reflected in a corresponding rise in electricity consumption from the utility grid. The current flowing across each generation unit and load is shown in

Figure 16(b). The grid frequency matches the inverter output frequency of 50 Hz as shown in Figure 17(a). Figure 17(b) illustrates the waveforms of the inverter's output voltage as well as its output current. As seen in Figure 18, the authorized ThingSpeak platform uses energy-internet technology to report power-balanced outcomes.

Figures 19–21 show the system outcomes with the applied DSM. Figure 19 illustrates the power of every load and generation resource. It is clear from Figure 19(a) that the power purchased from the utility grid is reduced in comparison without adopting DSM (Figure 16(a)). Figure 20(a) illustrates the frequency response of the grid and inverter output, while the inverter output current and voltage signals are shown in Figure 20(b). As shown in Figure 21, the ThingSpeak platform uses EI technology to illustrate balanced load-generation power. Figures 22(a) and 22(b) show the adopted real-time price (in the top) and the cost of the system's energy use (in the bottom) without and with adopting DSM, respectively. Figures 23(a) and 23(b) illustrated the price signal and consumption cost results displayed on ThinkSpeak platform without and with adopting DSM, respectively. It is evident that both utility power use and energy consumption costs have decreased by adopting DSM. Figure 24 shows the electricity bill per month without the adopted DSM (unscheduled load profile in the red column) and with the adopted DSM (green column for BSOA-based DSM, yellow for SSA-based DSM, and black for CSA-based DSM). The unscheduling load profile requires a monthly payment of 484.4 $, whereas all of the algorithms in the adopted DSM reduce the monthly electricity bill to 439.1 $.

4.4. Test 4: AC Load Change during Islanded Mode Transition with PR and PI Controllers Comparison. In the test 4, the system is in grid-connected mode. The MG is then operated
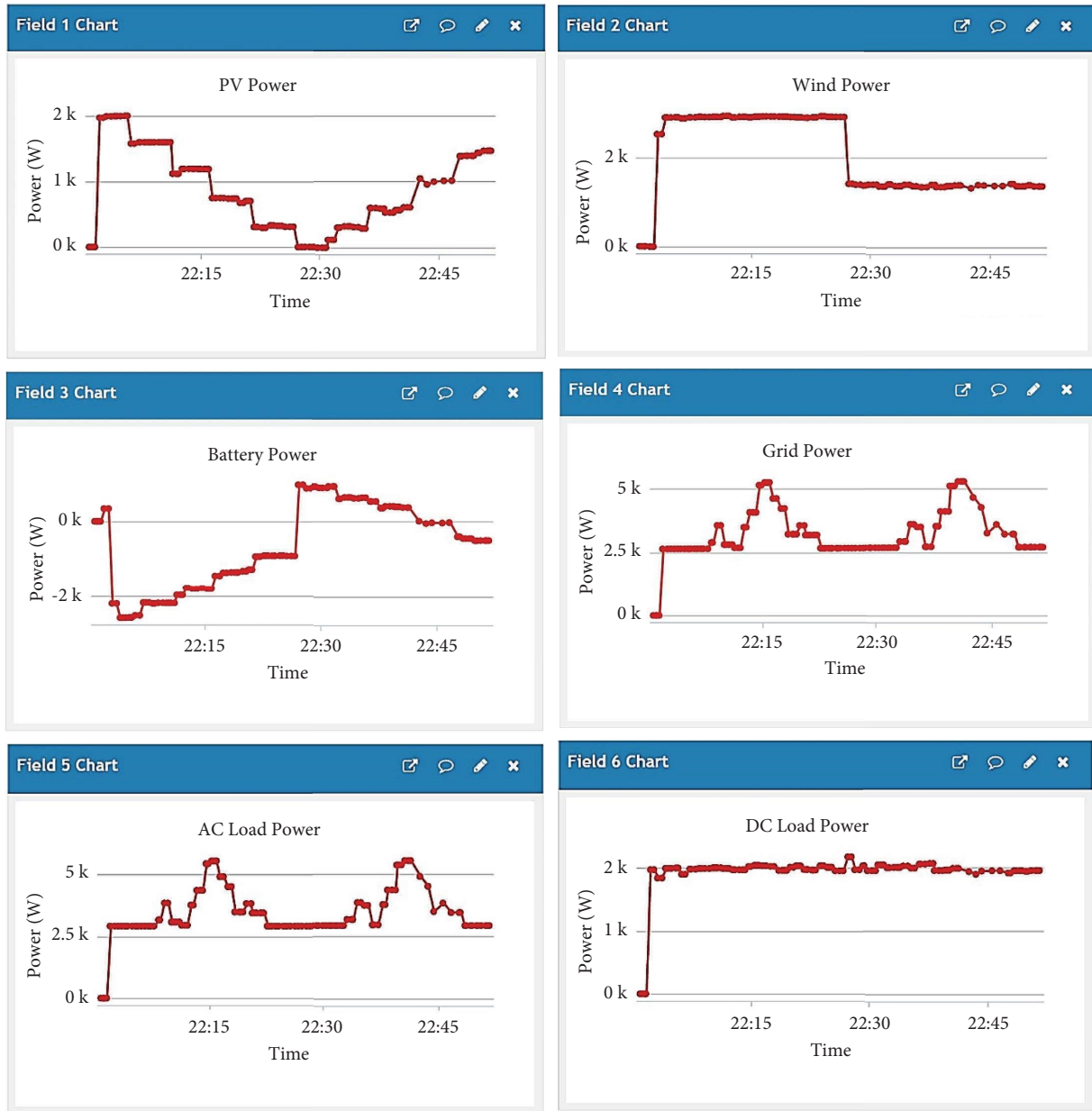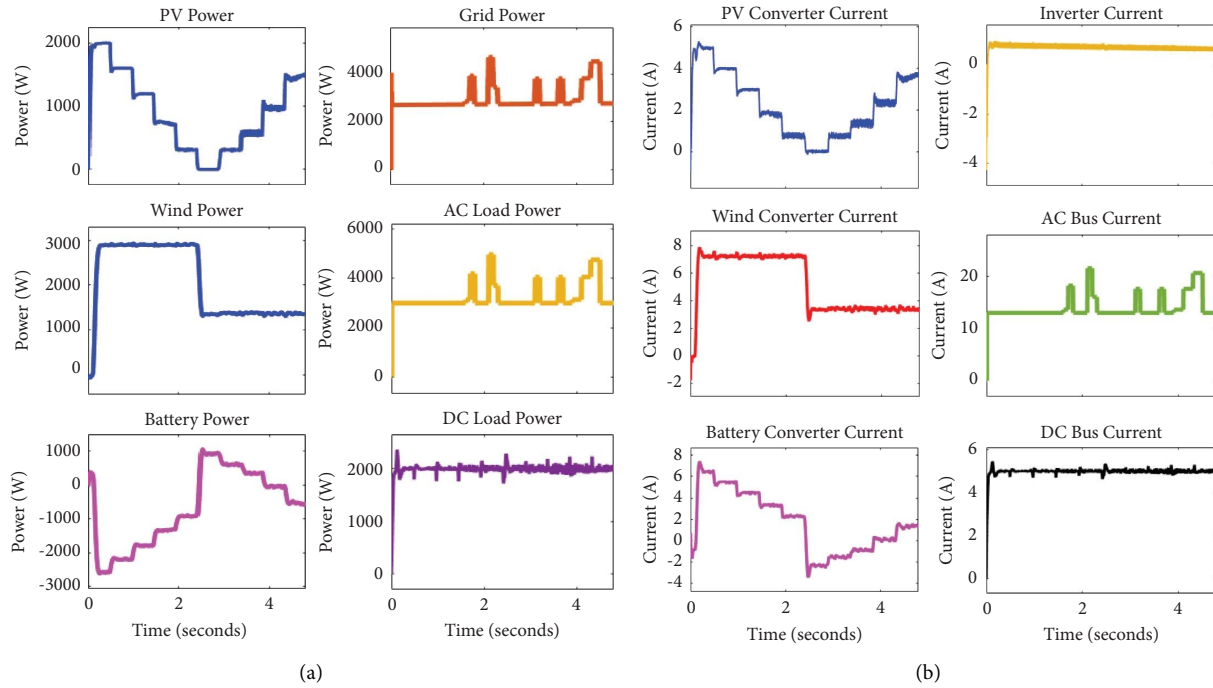
Figure 18: The results of system power, price signal, and energy costs displayed on ThingSpeak platform without adopting DSM.

in island mode at 3 sec time point, and at the time point of 4 sec, the AC load power is increased to up to 600 W. As shown in Figure 25(a), the generating-load power balance is kept. The current of every source and load is illustrated in Figure 25(b). At the 4 sec mark, the AC load increases to 600 W, indicating that the inverter current increases at this time. The currents of the generation units, including PV, WT, and storage systems, follow their power, as shown in Figure 25(a). In grid-connected mode, as seen in Figure 26(a), the grid frequency is at its nominal value (50 Hz), and the inverter output frequency is maintained at

this value in island mode of operation as well. The inverter's voltage and current are pure sinewaves as shown in Figure 26(b). The inverter output voltage remains constant at 312 V at time point (4 sec), while the current increases due to an increase in AC load.

Using the discrete PR controller-based proposed control, the output voltage and current waveforms of the inverter are pure sinusoidal without ripple (zero steady-state error), as seen in Figure 26. Using PI controllers instead of PR controllers leads to distorted output waveforms, as seen in Figure 27.

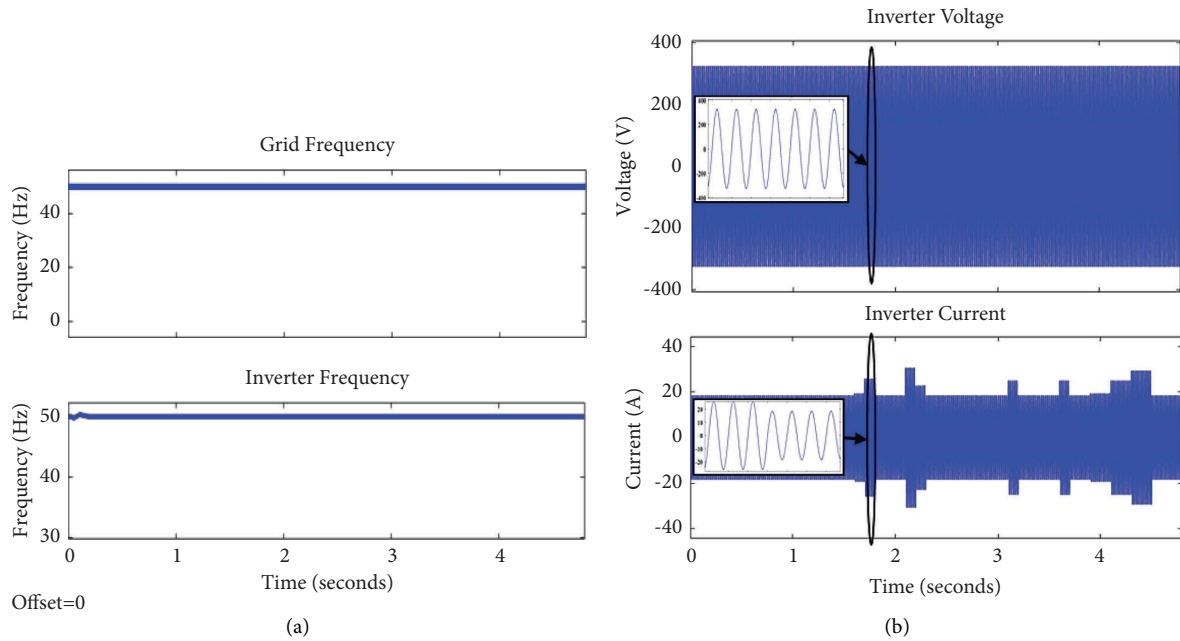FIGURE 19: (a) Load-generation powers and (b) load-generation currents using DSM.

FIGURE 20: (a) Grid and inverter frequencies and (b) inverters' output voltage and current waveforms with applying DSM.
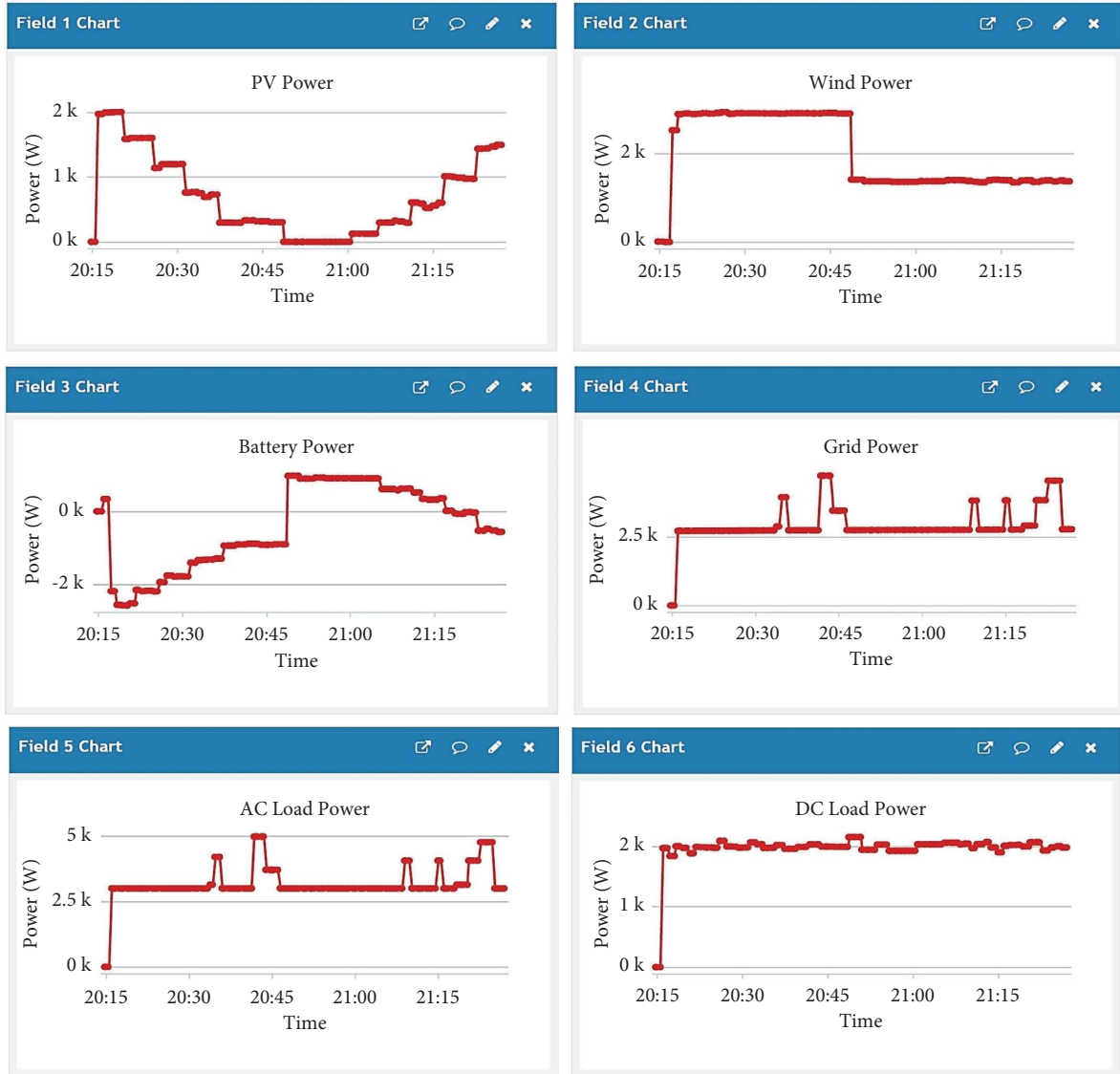
FIGURE 21: The results of system power, price signal, and energy costs displayed on ThingSpeak platform with adopting DSM.
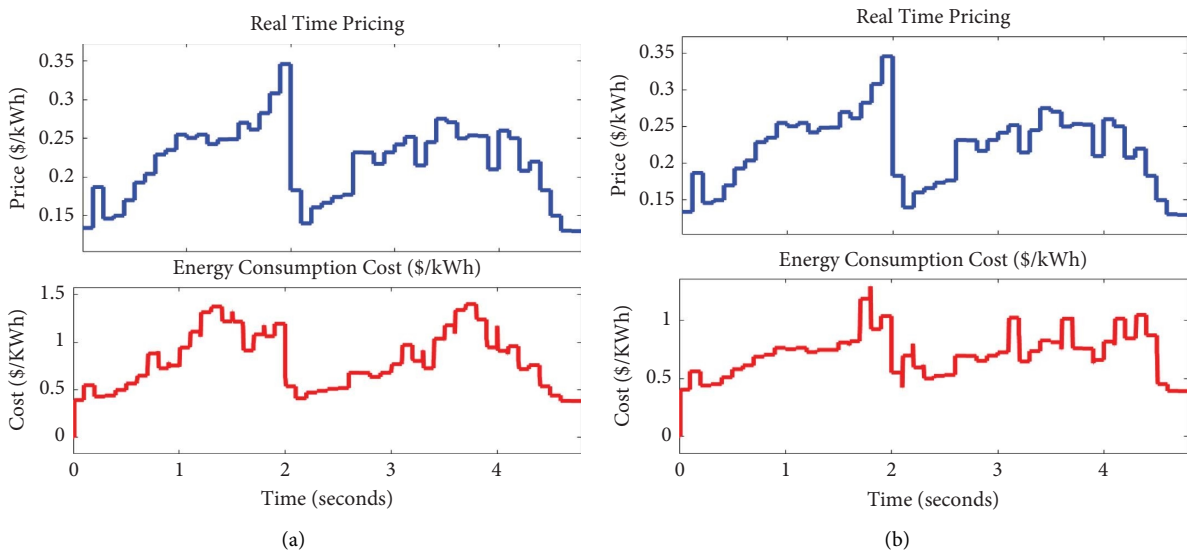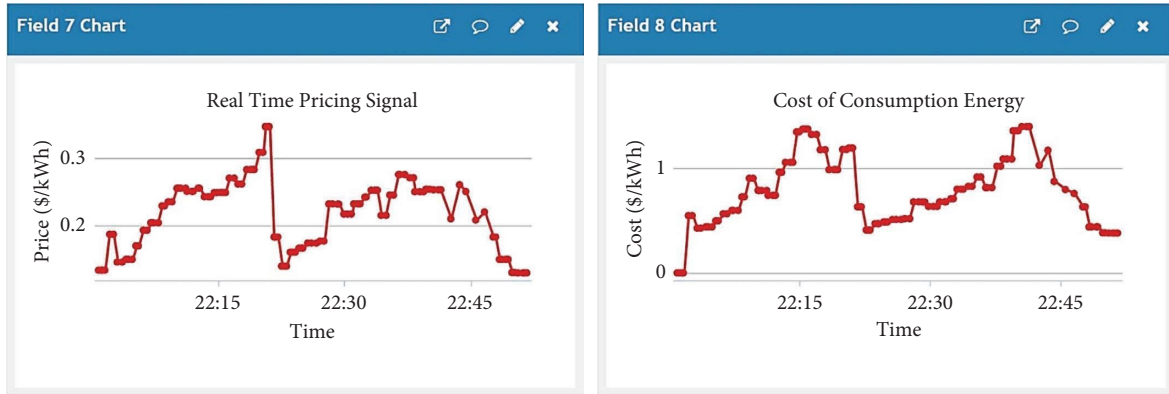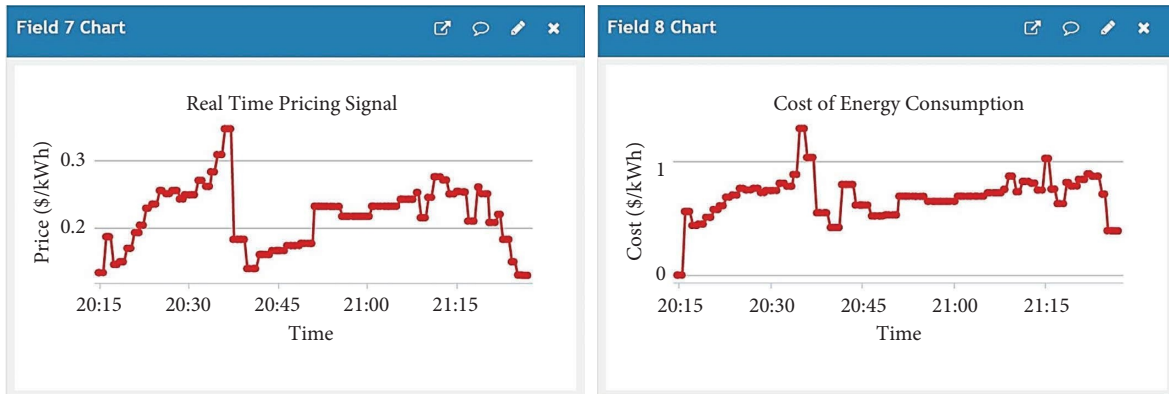

FIGURE 22: The adopted real-time price and the energy consumption cost (a) without applying DSM and (b) with applying DSM.

(a)

(b)

FIGURE 23: The adopted real-time price and the energy consumption cost displayed on ThingSpeak platform (a) without applying DSM and (b) with applying DSM.
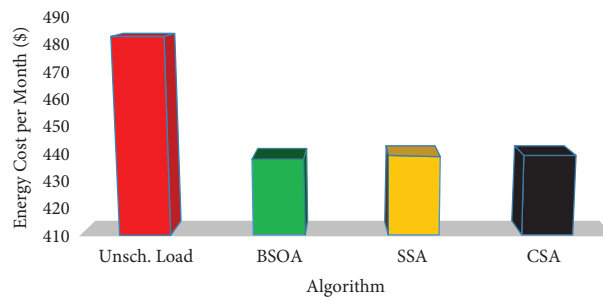

FIGURE 24: The costs of electricity bill per month with and without adopting DSM.
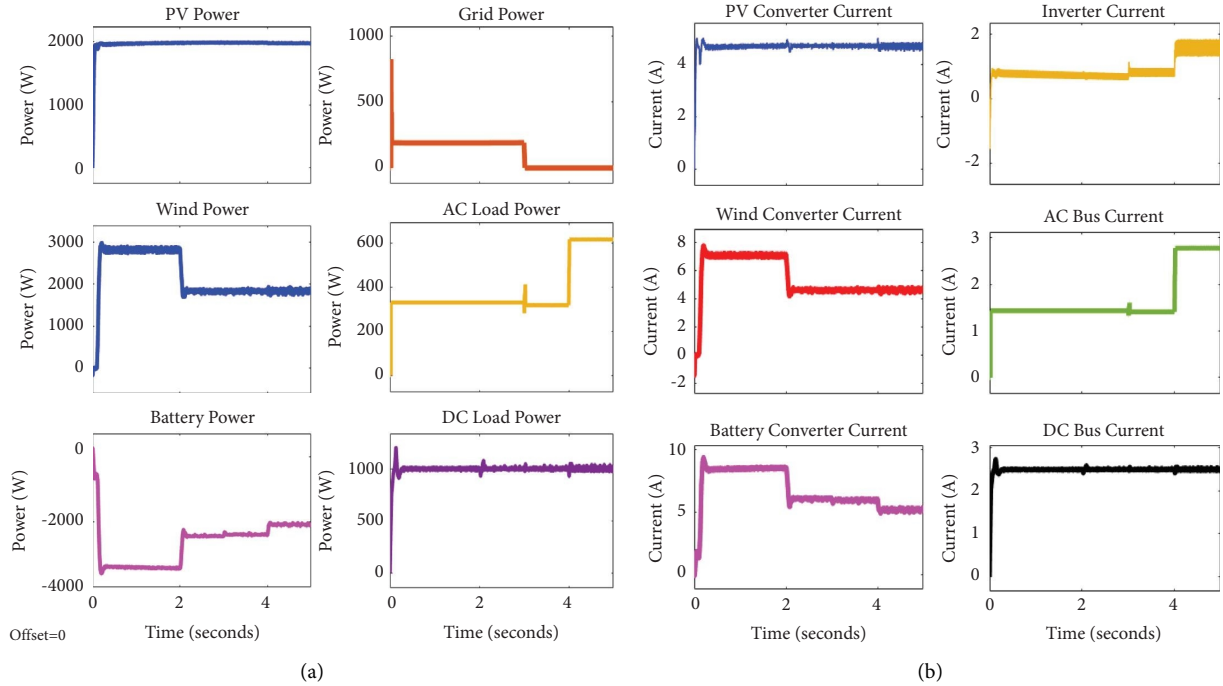
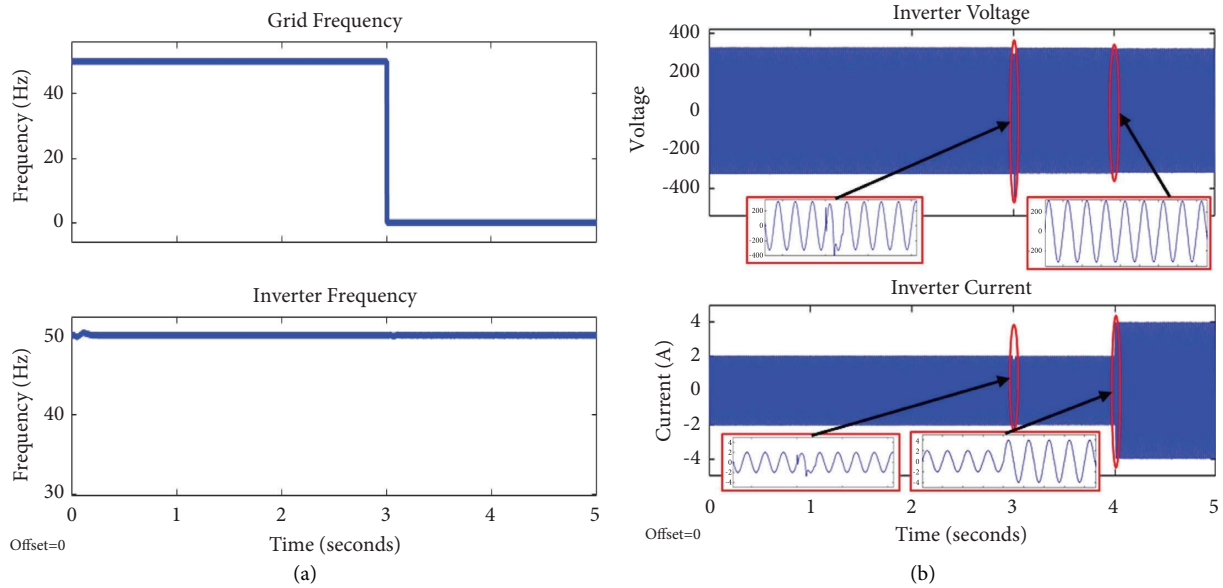FIGURE 25: (a) Load-generation powers and (b) load-generation currents in test 4.

FIGURE 26: (a) Grid and inverter frequencies and (b) inverters' output voltage and current waveforms using PR controllers in test 4.
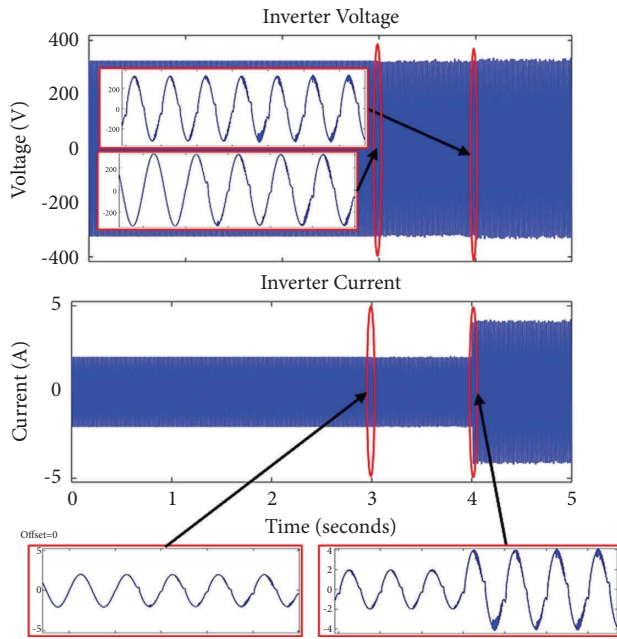
FIGURE 27: Inverter's output voltage and current waveforms using PI controllers in test 4.

has dropped, the load factor (1/peak-to-average) has improved. The nonscheduling load profile costs 484.4 $ per month, whereas all adopted DSM algorithms lower the expense to 439.1 $.

In order to further and efficiently reduce power use, the paper recommends future studies that include the use of peak clipping DSM technique with load shifting-based technique, priority operation devices, and incorporating packet loss.

Data Availability

No data were used to support this study.

Conflicts of Interest

The authors declare that they have no conflicts of interest.

Acknowledgments

5. Conclusion

The instability of renewable energy-based MG increases with the penetration of renewable resources. By balancing energy generation and consumption, this instability can be addressed. This paper studies the penetration of co-ordination control to ensure MG stability under changeable load and generation conditions and addresses the problem of coordinated power flow between the main grid and MG buses. The bidirectional main DC/AC converter of the adopted system is managed by applying a control strategy that utilizes digital PR controllers, which effectively provide pure sinewave voltage output signals with zero oscillations, which makes them superior in comparison with the adopting PI controllers, as illustrated in the system results. This work proposes a hybrid MPPT technique using an ANFIS and PSO to adapt the output of traditional perturb and observe and incremental conductance methods in order to maximize solar PV power with zero fluctuation tracking against the system's nonlinearity. Regarding the management system, an optimal program of demand management based on meta-heuristic algorithms (SSA, BSOA, and CSA) has been adopted to adjust the end-user power consumption. Lastly, based on energy Internet technology, ThingSpeak cloud-based MATLAB is adopted to gather and display real-time data streams and generate graphical analyses. The simulation results prove that our proposed control maintains the dynamic stability of MG, achieves power balance, reduces electricity consumption, and satisfies load demand. The suggested coordinating control outperforms the proportional integral-based technique in steady state with zero error and a fast grid frequency response. With optimal demand management, it reduces the peak energy demand from 5.2 kWh to 4.6 kWh. Since peak consumption

References

[1] A. M. Jasim, B. H. Jasim, B.-C. Neagu, and B. N. Alhasnawi, "Efficient optimization algorithm-based demand-side management program for smart grid residential load," *Axioms*, vol. 12, no. 1, p. 33, 2022.

[2] A. M. Jasim, B. H. Jasim, F. Aymen, H. Kotb, and A. Althobaiti, "Consensus-based intelligent distributed secondary control for multiagent islanded microgrid," *International Transactions on Electrical Energy Systems*, vol. 2023, Article ID 6812351, 20 pages, 2023.

[3] M. Silva, F. Fernandes, H. Morais, S. Ramos, and Z. Vale, "Hour-ahead energy resource management in university campus microgrid," in *Proceedings of the 2015 IEEE Eindhoven PowerTech*, pp. 1–6, Eindhoven, The Netherlands, July 2015.

[4] V. Machamint, K. Oureilidis, V. V. Venizelou, and G. E. Efthymiou, "Optimal energy storage sizing of a microgrid under different pricing schemes," in *Proceedings of the 2018 IEEE 12th International Conference Compatibility Power Electronics and Power Engineering, CPE-POWERENG*, pp. 1–6, Doha, Qatar, April 2018.

[5] J. Singh and R. Behera, "Hysteresis current controllers for grid connected inverter: review and experimental implementation," in *Proceedings of the IEEE International Conference on Power Electronics, Drives and Energy Systems (PEDES)*, Chennai, India, December 2018.

[6] G. Elhassan, S. A. Zulkifli, S. Z. Iliya et al., "Deadbeat current control in grid-connected inverters: a comprehensive discussion," *IEEE Access*, vol. 10, pp. 3990–4014, 2022.

[7] A. M. Jasim, B. H. Jasim, B.-C. Neagu, and B. N. Alhasnawi, "Coordination control of a hybrid AC/DC smart microgrid with online fault detection, diagnostics, and localization using

artificial neural networks," *Electronics*, vol. 12, no. 1, p. 187, 2022.

[8] J. R. R. Zientarski, M. L. D. S. Martins, J. R. Pinheiro, and H. L. Hey, "Series-connected partial-power converters applied to PV systems: a design approach based on step-up/down voltage regulation range," *IEEE Transactions on Power Electronics*, vol. 33, no. 9, pp. 7622–7633, 2018.

[9] M. Jedari Zare Zadeh and S. H. Fathi, "A new approach for photovoltaic arrays modeling and maximum power point estimation in real operating conditions," *IEEE Transactions on Industrial Electronics*, vol. 64, no. 12, pp. 9334–9343, 2017.

[10] F. El Aamri, H. Maker, D. Sera, S. V. Spataru, J. M. Guerrero, and A. Mouhsen, "A direct maximum power point tracking method for singlephase grid-connected PV inverters," *IEEE Transactions on Power Electronics*, vol. 33, no. 10, pp. 8961–8971, 2018.

[11] A. Costa de Souza, F. Cardoso Melo, T. Lima Oliveira, and C. Eduardo Tavares, "Performance analysis of the computational implementation of a simplified PV model and MPPT algorithm," *IEEE Latin America Transactions*, vol. 14, no. 2, pp. 792–798, 2016.

[12] O. Khan, S. Acharya, M. Al Hosani, and M. S. El Moursi, "Hill climbing power flow algorithm for hybrid DC/AC microgrids," *IEEE Transactions on Power Electronics*, vol. 33, no. 7, pp. 5532–5537, 2018.

[13] D. C. Huynh and M. W. Dunnigan, "Development and comparison of an improved incremental conductance algorithm for tracking the MPP of a solar PV panel," *IEEE Transactions on Sustainable Energy*, vol. 7, no. 4, pp. 1421–1429, 2016.

[14] N. Kumar, I. Hussain, B. Singh, and B. K. Panigrahi, "Framework of maximum power extraction from solar PV panel using self predictive perturb and observe algorithm," *IEEE Transactions on Sustainable Energy*, vol. 9, no. 2, pp. 895–903, 2018.

[15] A. G. Al-Gizi, A. Craciunescu, and S. J. Al-Chlaihawi, "The use of ANN to supervise the PV MPPT based on FLC," in *Proceedings of the 2017 10th International Symposium on Advanced Topics in Electrical Engineering (ATEE)*, pp. 703–708, Bucharest, Romania, March 2017.

[16] R. B. A. Koad, A. F. Zobaa, and A. El-Shahat, "A novel MPPT algorithm based on particle swarm optimization for photovoltaic systems," *IEEE Transactions on Sustainable Energy*, vol. 8, no. 2, pp. 468–476, 2017.

[17] N. A. Windarko, A. Tjahjono, D. O. Anggriawan, and M. H. Purnomo, "Maximum power point tracking of photovoltaic system using adaptive modified firefly algorithm," in *Proceedings of the 2022 International Electronics Symposium (IES)*, pp. 31–35, Surabaya, Indonesia, September 2015.

[18] K. Sundareswaran, V. Vigneshkumar, P. Sankar, S. P. Simon, P. Srinivasa Rao Nayak, and S. Palani, "Development of an improved P&O algorithm assisted through a colony of foraging ants for MPPT in PV system," *IEEE Transactions on Industrial Informatics*, vol. 12, no. 1, pp. 187–200, 2016.

[19] K. Sundareswaran, P. Sankar, P. S. R. Nayak, S. P. Simon, and S. Palani, "Enhanced energy output from a PV system under partial shaded conditions through artificial bee colony," *IEEE Transactions on Sustainable Energy*, vol. 6, no. 1, pp. 198–209, 2015.

[20] N. Priyadarshi, S. Padmanaban, P. Kiran Maroti, and A. Sharma, "An extensive practical investigation of FPSO-based MPPT for grid integrated PV system under variable operating conditions with anti-islanding protection," *IEEE Systems Journal*, vol. 13, no. 2, pp. 1861–1871, 2019.

[21] P. Chittaranjan, S. M. Kumar, M. S. Ganesh, N. P. Kumar, and G. Terje, "Coordinated power management and control of standalone PV-hybrid system with modified IWO-based MPPT," *IEEE Systems Journal*, vol. 15, no. 3, pp. 1–12, 2020.

[22] S. M. Kumar, P. Chittaranjan, and R. K. Calay, "Computational intelligence based maximum power point tracking for photovoltaic power generation system with small-signal analysis," *Optimal Control Applications and Methods*, vol. 44, no. 1, 2021.

[23] Z. Chen, J. Chen, K. Fu, and L. Xue, "Power coordination control strategy of microgrid based on photovoltaic generation," *MATEC Web of Conferences*, vol. 355, p. 3065, 2022.

[24] H. Hui, Y. Chen, S. Yang, H. Zhang, and T. Jiang, "Coordination control of distributed generators and load resources for frequency restoration in isolated urban microgrids," *Applied Energy*, vol. 327, Article ID 120116, 2022.

[25] M. Eslami, M. Neshat, and S. A. Khalid, "A novel hybrid sine cosine algorithm and pattern search for optimal coordination of power system damping controllers," *Sustainability*, vol. 14, no. 1, p. 541, 2022.

[26] A. Zahernia and H. Rahbarimagham, "Application of smart transformers in power systems including PV and storage systems under unbalanced and nonlinear load and fault condition," *Electric Power Systems Research*, vol. 201, Article ID 107535, 2021.

[27] L. O. Mogaka, G. N. Nyakoe, and M. J. Saulo, "Islanded and grid-connected control in a microgrid with wind-PV hybrid," *International Journal of Applied Engineering Research*, vol. 15, no. 4, pp. 352–357, 2020.

[28] B. N. Alhasnawi and B. H. Jasim, "Adaptive energy management system for smart hybrid microgrids," in *Proceedings of the 3rd Scientific Conference of Electrical and Electronic Engineering Researches*, pp. 15-16, Basrah, Iraq, June 2020.

[29] A. Jasim and B. Jasim, "Grid-forming and grid-following based microgrid inverters control," *Iraqi Journal for Electrical and Electronic Engineering*, vol. 18, no. 1, pp. 111–131, 2022.

[30] I. V. Banu, R. Beniugă, and M. Istrate, "Comparative analysis of the perturb-and-observe and incremental conductance MPPT methods," in *Proceedings of the 2013 8th International Symposium on Advanced Topics in Electrical Engineering (ATEE)*, pp. 1–4, Bucharest, Romania, May 2013.

[31] B. Alhasnawi and B. H. Jasim, "A new coordinated control of hybrid microgrids with renewable energy resources under variable loads and generation conditions," *Iraqi Journal for Electrical and Electronic Engineering*, vol. 16, no. 2, pp. 1–20, 2020.

[32] U. Akram and M. Khalid, "A coordinated frequency regulation framework based on hybrid battery-ultracapacitor energy storage technologies," *IEEE Access*, vol. 6, pp. 7310–7320, 2018.

[33] J. K. Singh and R. K. Behera, "Hysteresis current controllers for grid connected inverter: review and experimental implementation," in *Proceedings of the 2022 IEEE International Conference on Power Electronics, Drives and Energy Systems (PEDES)*, pp. 1–6, Jaipur, India, December 2018.

[34] M. J. Ali, H. J. Basil, B. Vladimir, and P. Mikulecky, "A novel cooperative control technique for hybrid AC/DC smart microgrid converters," *IEEE Access*, vol. 11, pp. 2164–2181, 2023.

[35] N. Zhang, H. Tang, and C. Yao, "A systematic method for designing a PR controller and active damping of the LCL filter for single-phase grid-connected PV inverters," *Energies*, vol. 7, no. 6, pp. 3934–3954, 2014.

[36] S. A. A. Fallahzadeh, N. R. Abjadi, A. Kargar, and F. Blaabjerg, "Applying sliding-mode control to a double-stage single-phase grid-connected PV system," *Journal of Renewable Energy and Environment*, vol. 8, pp. 1–12, 2021.

[37] M. K. Senapati, C. Pradhan, S. R. Samantaray, and P. K. Nayak, "Improved power management control strategy for renewable energy-based DC micro-grid with energy storage integration," *IET Generation, Transmission & Distribution*, vol. 13, no. 6, pp. 838–849, 2018.

[38] A. Bayo-Salas, J. Beerten, J. Rimez, and D. Van Hertem, "Analysis of control interactions in multi-infeed VSC HVDC connections," *IET Generation, Transmission & Distribution*, vol. 10, no. 6, pp. 1336–1344, 2016.

[39] G.-J. Li, S.-Y. Ruan, B.-T. Ooi, Y.-Z. Sun, and S. S. Choi, "Autonomous AC grid based on multi-infeed voltage source converter stations," *Electric Power Components and Systems*, vol. 38, no. 5, pp. 558–574, 2010.

[40] M. S. Sadabadi and Q. Shafiee, "Decentralized multivariable vector current control of grid-connected voltage source inverters," *IFAC-PapersOnLine*, vol. 53, no. 2, pp. 12410–12415, 2020.

[41] A. M. Jasim, B. H. Jasim, and B.-C. Neagu, "A new decentralized PQ control for parallel inverters in grid-tied microgrids propelled by SMC-based buck–boost converters," *Electronics*, vol. 11, no. 23, p. 3917, 2022.

[42] G. H. Philipo, J. N. Kakande, and S. Krauter, "Neural network-based demand-side management in a stand-alone solar PV-battery microgrid using load-shifting and peak-clipping," *Energies*, vol. 15, no. 14, p. 5215, 2022.

[43] K. Miyazaki, K. Kobayashi, S.-I. Azuma, N. Yamaguchi, and Y. Yamashita, "Design and value evaluation of demand response based on model predictive control," *IEEE Transactions on Industrial Informatics*, vol. 15, no. 8, pp. 4809–4818, 2019.

[44] V. A. Freire, L. V. R. De Arruda, C. Bordons, and J. J. Márquez, "Optimal demand response management of a residential microgrid using model predictive control," *IEEE Access*, vol. 8, pp. 228264–228276, 2020.

[45] A. M. Jasim, B. H. Jasim, S. Mohseni, and A. C. Brent, "Consensus-based dispatch optimization of a microgrid considering MetaHeuristic-based demand response scheduling and network packet loss characterization," *Energy and AI*, vol. 11, Article ID 100212, 2023.

[46] A. M. Jasim, B. H. Jasim, S. Mohseni, and A. C. Brent, "Energy internet-based load shifting in smart microgrids: an experimental study," *Energies*, vol. 16, no. 13, p. 4957, 2023.

[47] M. Waseem, Z. Lin, S. Liu, I. A. Sajjad, and T. Aziz, "Optimal GWCSO-based home appliances scheduling for demand response considering end-users comfort," *Electric Power Systems Research*, vol. 187, Article ID 106477, 2020.

[48] M. Noroozi, H. Mohammadi, E. Efatinasab, A. Lashgari, M. Eslami, and B. Khan, "Golden search optimization algorithm," *IEEE Access*, vol. 10, pp. 37515–37532, 2022.

[49] D. Mohammad, M. Zeinab, P. M. Om, D. Gaurav, and K. Vijay, "BOSA: binary orientation search algorithm," *International Journal of Innovative Technology and Exploring Engineering*, vol. 9, pp. 5306–5310, 2019.

[50] A. Fathy, T. M. Alanazi, H. Rezk, and D. Yousri, "Optimal energy management of micro-grid using sparrow search algorithm," *Energy Reports*, vol. 8, pp. 758–773, 2022.

[51] I. Obagbuwa and A. Abidoye, "Binary cockroach swarm optimization for combinatorial optimization problem," *Algorithms*, vol. 9, no. 3, p. 59, 2016.

[52] B. N. Alhasnawi, B. H. Jasim, Z.-A. S. A. Rahman, J. M. Guerrero, and M. D. Esteban, "A novel internet of energy based optimal multi-agent control scheme for microgrid including renewable energy resources," *International Journal of Environmental Research and Public Health*, vol. 18, no. 15, p. 8146, 2021.

[53] G. Shabib, E. H. Abd-Elhameed, and G. Magdy, "A new approach to the digital implementation of analog controllers for a power system control," *International Journal of Scientific Engineering and Research*, vol. 5, pp. 1–9, 2014.

[54] J. Ali et al, J. Mahmood, and R. Salim, "Design and implementation of a musical water fountain based on sound harmonics using IIR filters," *International Journal of Computing and Digital Systems*, vol. 9, no. 2, pp. 319–333, 2020.

[55] S. Bacha, I. Munteanu, and A. Bratcu, "Power electronic converters modeling and control," *Part of the Book Series: Advanced Textbooks in Control and Signal Processing (C&SP)*, Vol. 454, Springer, Berlin, Germany, 2013.

[56] N. Priyadarshi, S. Padmanaban, J. B. Holm-Nielsen, F. Blaabjerg, and M. S. Bhaskar, "An experimental estimation of hybrid ANFIS–PSO-based MPPT for PV grid integration under fluctuating sun irradiance," *IEEE Systems Journal*, vol. 14, no. 1, pp. 1218–1229, 2020.

[57] L. Nieto and J. M. Diseño, *Simulación de un Regulador de Histéresis con Frecuencia de Conmutación Fija*, Ph.D. thesis, Universitat Politecnica de Catalunya, Barcelona, Spain, 2007.

[58] K. H. Chao, M. C. Tseng, C. H. Huang, Y. G. Liu, and L. C. Huang, "Design and implementation of a bidirectional DC-DC converter for stand-alone photovoltaic systems," *International Journal of Computers, Communications & Control*, vol. 2, no. 12, 2013.

[59] J. Xue and B. Shen, "A novel swarm intelligence optimization approach: sparrow search algorithm," *Systems Science & Control Engineering*, vol. 8, no. 1, pp. 22–34, 2020.

[60] Z. Chen and H. Tang, "Cockroach swarm optimization for vehicle routing problems," *Energy Procedia*, vol. 13, pp. 30–35, 2011.

[61] L. Cheng, Z. Wang, Y. H. Song, and A. Guo, "Cockroach swarm optimization algorithm for TSP," *Advanced Engineering Forum*, vol. 1, pp. 226–229, 2011.

[62] J. Kwiecień and M. Pasieka, "Cockroach swarm optimization algorithm for travel planning," *Entropy*, vol. 19, no. 5, p. 213, 2017.

[63] C. ZhaoHui and T. HaiYan, "Cockroach swarm optimization," in *Proceedings of the 2nd International Conference on Computer Engineering and Technology (ICCET '10)*, vol. 6, pp. 652–655, Chengdu, China, April 2010.

[64] I. Obagbuwa and A. Adewumi, "An improved cockroach swarm optimization," *The Scientific World Journal*, vol. 2014, Article ID 375358, 13 pages, 2014.